

# Kilometer-scale simulations of trade-wind cumulus capture processes of mesoscale organization

Leo Saffin<sup>1</sup>, Adrian Lock<sup>2</sup>, Lorenzo Tomassini<sup>2</sup>, Alan Blyth<sup>1,3</sup>, Steven Böing<sup>1</sup>,  
Leif Denby<sup>1</sup>, and John Marsham<sup>1</sup>

<sup>1</sup>University of Leeds, UK

<sup>2</sup>Met Office, UK

<sup>3</sup>NCAS, UK

## Key Points:

- Kilometer-scale UM simulations capture an increase in mesoscale organization associated with an observed “flowers” cloud pattern
- The time window during which clouds and mesoscale organization develop is associated with large-scale moisture convergence
- Initial organization and cold pools have little effect on timing and cold pools only have a small opposing effect to mesoscale organization

## Abstract

The international field campaign for EUREC<sup>4</sup>A (Elucidating the role of clouds–circulation coupling in climate) gathered observations to better understand the links between trade-wind cumulus clouds, their organization, and larger scales, a large source of uncertainty in climate projections. A recent large-eddy simulation (LES) study showed a cloud transition that occurred during EUREC<sup>4</sup>A (2<sup>nd</sup> February 2020), where small shallow clouds developed into larger clouds with detrainment layers, was caused by an increase in mesoscale organization generated by a dynamical feedback in mesoscale vertical velocities. We show that kilometer-scale simulations with the Met Office’s Unified Model reproduce this increase in mesoscale organization and the process generating it, despite being much lower resolution. The simulations develop mesoscale organization stronger and earlier than the LES, more consistent with satellite observations. Sensitivity tests with a shorter spin-up time, to reduce initial organization, still have the same timing of development and sensitivity tests with cold pools suppressed show only a small effect on mesoscale organization. These results suggest that large-scale circulation, associated with an increased vertical velocity and moisture convergence, is driving the increase in mesoscale organization, as opposed to a threshold reached in cloud development. Mesoscale organization and clouds are sensitive to resolution, which affects changes in net radiation, and clouds still have substantial differences to observations. Therefore, while kilometer-scale simulations can be useful for understanding processes of mesoscale organization and links with large scales, including responses to climate change, simulations will still suffer from significant errors and uncertainties in radiative budgets.

## Plain Language Summary

A recent field campaign, EUREC<sup>4</sup>A (Elucidating the role of clouds–circulation coupling in climate), made extensive measurements of shallow clouds upstream of Barbados and the surrounding region. These clouds are important because their effect on climate change is highly uncertain. When looking at the cloud patterns in satellite images, we can see that the patterns they form can vary dramatically. One example from EUREC<sup>4</sup>A, 2<sup>nd</sup> February 2020, is when the clouds changed from a region of small clouds that looks like a scattering of sugar in satellite images to larger patches of clouds that look like flow-ers separated by patches of clear sky. A previous study with a very high resolution model has shown the physical mechanism behind this change in the cloud pattern. We have shown

that lower resolution simulations can reproduce this transition from 2<sup>nd</sup> February and the physical mechanism associated with it. The trade off with low resolution is that it allows us to use a much larger domain and therefore capture features of the atmospheric flow on larger scales. This benefit of domain size is seen in the ability of the simulations to capture the timing of the change in cloud pattern. However, the low resolution means that the development of individual clouds is poorly represented which can be seen in the differences between the modeled cloud structures and observations. The results show how the model is a useful testbed for better understanding the physical mechanism behind changes in cloud patterns and what might affect it, but the impacts of clouds on climate, via reflecting sunshine and absorbing infrared radiation, will still have large errors and uncertainties in climate projections.

## 1 Introduction

The modeled response of trade-wind cumulus to climate change is highly uncertain, leading to large uncertainties in the radiative feedback and resulting climate sensitivity (Bony & Dufresne, 2005). This uncertainty is linked to the inability of models to capture the relationship between cloud cover and the large-scale circulation (Nuijens et al., 2015a). Observations of trade-wind clouds show that the strongest variability comes from stratiform regions at 1.5-2 km on timescales of a few hours with less variability at the cloud base (Nuijens et al., 2014); however, models capture climatological-mean cloud cover as the combination of many unrealistic states (Nuijens et al., 2015a). This was shown to be because models too strongly relate cloud cover to single large-scale parameters, such as mixed-layer relative humidity or inversion strength (Nuijens et al., 2015b), whereas in reality, the dependence of cloud cover on the large-scale circulation is more complex and can't be predicted by a single parameter on synoptic timescales (Brueck et al., 2015). High climate sensitivity arises when warming leads to an increased convective mixing which can lead to a reduction in the amount of low clouds; however, this response is strongly dependent on the formulation of convection and can be related to the representation of present-day clouds and convection in the model (Vial et al., 2016).

The need to better understand the links between clouds and the large-scale circulation motivated the EUREC<sup>4</sup>A (Elucidating the role of clouds–circulation coupling in climate) field campaign which took place in January–February 2020 (Bony et al., 2017; Stevens et al., 2021). A key result in the build up to EUREC<sup>4</sup>A was the classification

of different regimes of mesoscale organization in trade-wind cumulus clouds: Stevens et al. (2020) categorized cloud patterns from visible satellite images and found agreement on four distinct patterns of cloud organization, referred to as sugar, gravel, fish, and flowers. These patterns are useful because we can think about the variability in cloud cover in terms of transitions between these different regimes of cloud organization. The relevant example here being how a region of sugar, small and shallow clouds with little organization, can turn into a region of flowers, deeper clouds with large detrainment layers separated by cloud-free regions, over the course of a day, such as was observed during EUREC<sup>4</sup>A on 2<sup>nd</sup> February 2020.

The patterns of cloud organization have different cloud radiative effects and can largely be distinguished by large-scale parameters (surface winds and inversion strength) (Bony et al., 2020). So the objective of getting models to represent trade-wind cumulus well enough to be used for climate studies could be viewed as making sure models represent the different regimes of cloud organization and the variability between these regimes. However, the four patterns of trade-wind clouds represent extremes in a more continuous distribution (Janssens et al., 2021) and trade-wind clouds can be classified as a hierarchy of different regimes with distinct cloud structures and radiative effects (Denby, 2020).

To understand the physical processes generating cloud organization, high-resolution large-eddy simulations (LES) have been used to model trade-wind cumulus clouds. Bretherton and Blossey (2017) showed that organization in trade-wind cumulus can be generated solely by a dynamical feedback in latent-heat driven mesoscale vertical velocities: convection preferentially develops in moist regions and once convection develops, the circulation generated by the convection acts to converge moisture towards the existing convection, making moist regions moister and dry regions drier. While not crucial for the development of mesoscale organization, Bretherton and Blossey (2017) also showed that the interaction between clouds and radiation can speed up the initial development of mesoscale organization. It has also been shown that the interaction between clouds and radiation is important in developing the detrainment layers that are distinctive of the flowers regime (Vogel et al., 2019) even if they are not crucial for the development of organization.

Narenpitak et al. (2021) simulated the 2<sup>nd</sup> February case from EUREC<sup>4</sup>A using an LES driven by forcings following a Lagrangian trajectory (Lagrangian LES) and showed

that the development of the flowers was associated with the development of mesoscale organization generated by the mesoscale vertical velocities, consistent with Bretherton and Blossey (2017). In this study, we have looked at the same, 2<sup>nd</sup> February, case study from EUREC<sup>4</sup>A using high-resolution nested simulations with the Met Office’s unified model (UM).

Our simulations are at a high enough resolution to allow an explicit representation of convection, but at a much lower resolution than needed to resolve cloud processes such as entrainment, and at a much lower resolution than the LES previously used to study convective aggregation. While our simulations will not be as good at representing the cloud processes as LES, this is a trade-off with a much larger domain size. A large enough domain size has been shown to be important for correctly capturing mesoscale organization of trade-wind cumulus (Vogel et al., 2019). However, high-resolution LES are not currently possible at much larger domain sizes so are difficult to use to represent interactions between cloud organization and the large scale, or spatial variations in cloud organization over larger scales. These larger scale processes could be well represented in kilometer-scale simulations, provided they can represent the mesoscale organization. Since kilometer-scale simulations are being suggested for climate-change projections due to their improvements in the representation of precipitation (Kendon et al., 2014, 2019; Slingo et al., 2022), it is important to assess whether kilometer-scale simulations can capture these processes closely linked to uncertainties in climate sensitivity. In this study, we aim to address whether our simulations can represent the processes generating mesoscale organization and can therefore be used to better understand interactions between cloud organization and larger scales.

The layout of the paper is as follows. In section 2 the model simulations are described. In section 3.1 we introduce the idea of “quasi-Lagrangian domains” extracted from the UM simulations to better follow the development of mesoscale organization and compare with LES. In section 3.2 the mesoscale organization in the UM simulations is quantified across the different resolutions. In section 3.3 we quantify the processes responsible for the mesoscale organization following the analysis of Bretherton and Blossey (2017) and Narenpitak et al. (2021). In section 3.4 we quantify the effects of spin up on mesoscale organization in our simulations. In section 3.6 we quantify the sensitivity of large-scale averages to resolution and spin up. In section 4 we summarize the results from this study.

## 2 Model Data

We ran simulations with the Met Office’s Unified Model (UM) using the third iteration of the regional atmosphere and land configuration (RAL3). RAL3 is designed for nested models with resolutions fine enough for convection to be explicitly represented by the model dynamics and therefore has no convection parametrization. The first version of the regional atmosphere and land configuration (RAL1) is described in (Bush et al., 2020). Key differences between RAL1 and RAL3 of relevance here are that: i) RAL3 uses the two-moment Cloud–AeroSol Interacting Microphysics (CASIM) parametrization described by Miltenberger et al. (2018), ii) the parametrization of cloud fraction as a function of the gridbox mean state is done by the bimodal cloud scheme described by Weverberg et al. (2021), and iii) RAL3 includes “Leonard terms” in the turbulent mixing scheme which accounts for horizontal gradients of vertical velocity acting to tilt horizontal fluxes into the vertical (Hanley et al., 2019).

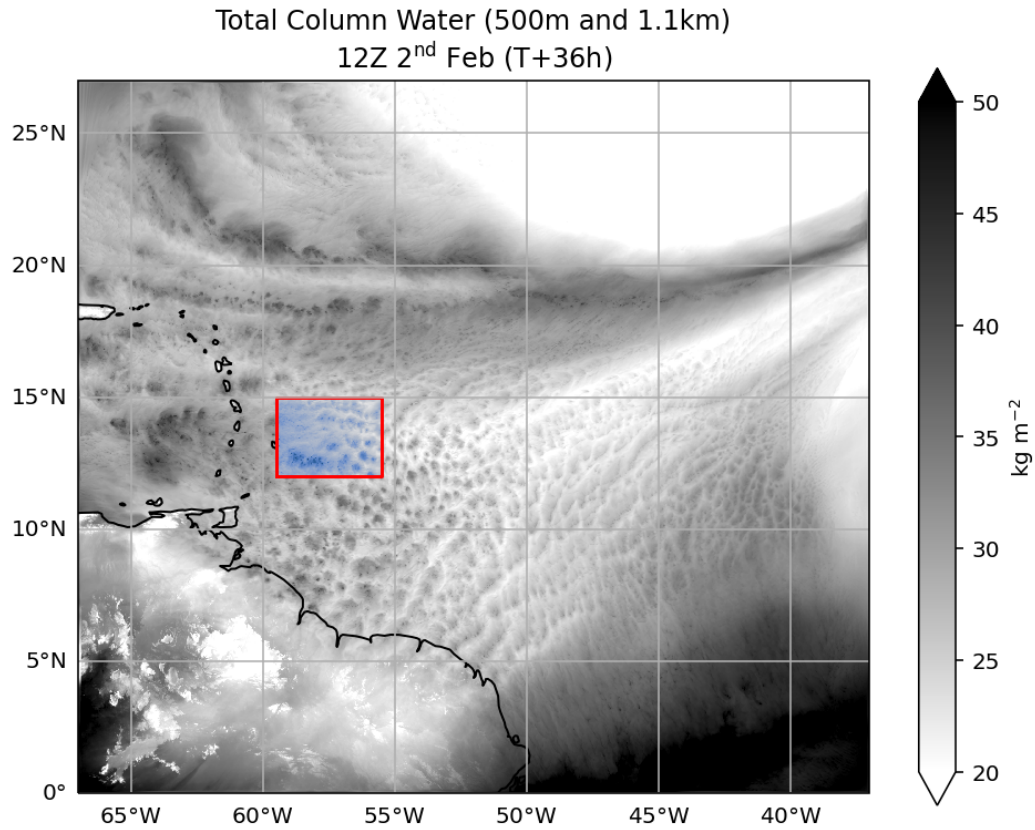
Kilometer-scale simulations (1.1, 2.2, and 4.4 km horizontal resolution) were initialized at 00Z 1<sup>st</sup> February and run for 48 hours. The initial conditions and boundary conditions are from ERA5 (Hersbach et al., 2020). ERA5 has an approximately 31 km horizontal resolution so clouds are not resolved in the initial conditions and are spun up in the UM simulations. Figure 1 shows the extent of the model domain. Higher-resolution simulations (300 m and 500 m horizontal resolution) were then nested within the 1.1 km simulation with the boundary conditions updated every 30 minutes. The box in Fig. 1 shows the extent of the nested domain. Table 1 gives a summary of the parameters that vary between simulations. To account for gray-zone issues with partially resolved eddies, the turbulent mixing scheme includes a resolution-dependent blending of the non-local fluxes (Boutle et al., 2014). Otherwise, each simulation used the same configuration (RAL3) and vertical resolution (70 hybrid-height levels decreasing in resolution from the surface up to 40 km).

## 3 Results

Figure 2 shows a comparison of the UM simulations with data from the GOES-16 satellite focused on the region of the inner domain. The model data is shown as the total outgoing longwave flux, whereas the satellite data is shown as brightness temperature from channel 11, which captures the water-vapor window in the infrared range. While

**Table 1.** Summary of simulations for 2<sup>nd</sup> February 2020 case from EUREC<sup>4</sup>A

Horizontal grid spacing	Boundary conditions	Timestep (s)	Grid (xy)
4.4km	ERA5	150	750 x 675
2.2km	ERA5	100	1500 x 1350
1.1km	ERA5	30	3000 x 2700
500m	1.1km run	30	800 x 600
300m	1.1km run	12	1350 x 1000

**Figure 1.** The domain of the UM simulations. Shown is a snapshot of total column water for the 1.1km simulation (outer domain) and 500m simulation (inner domain). The red box with the inside highlighted blue shows the boundaries of the inner domain.

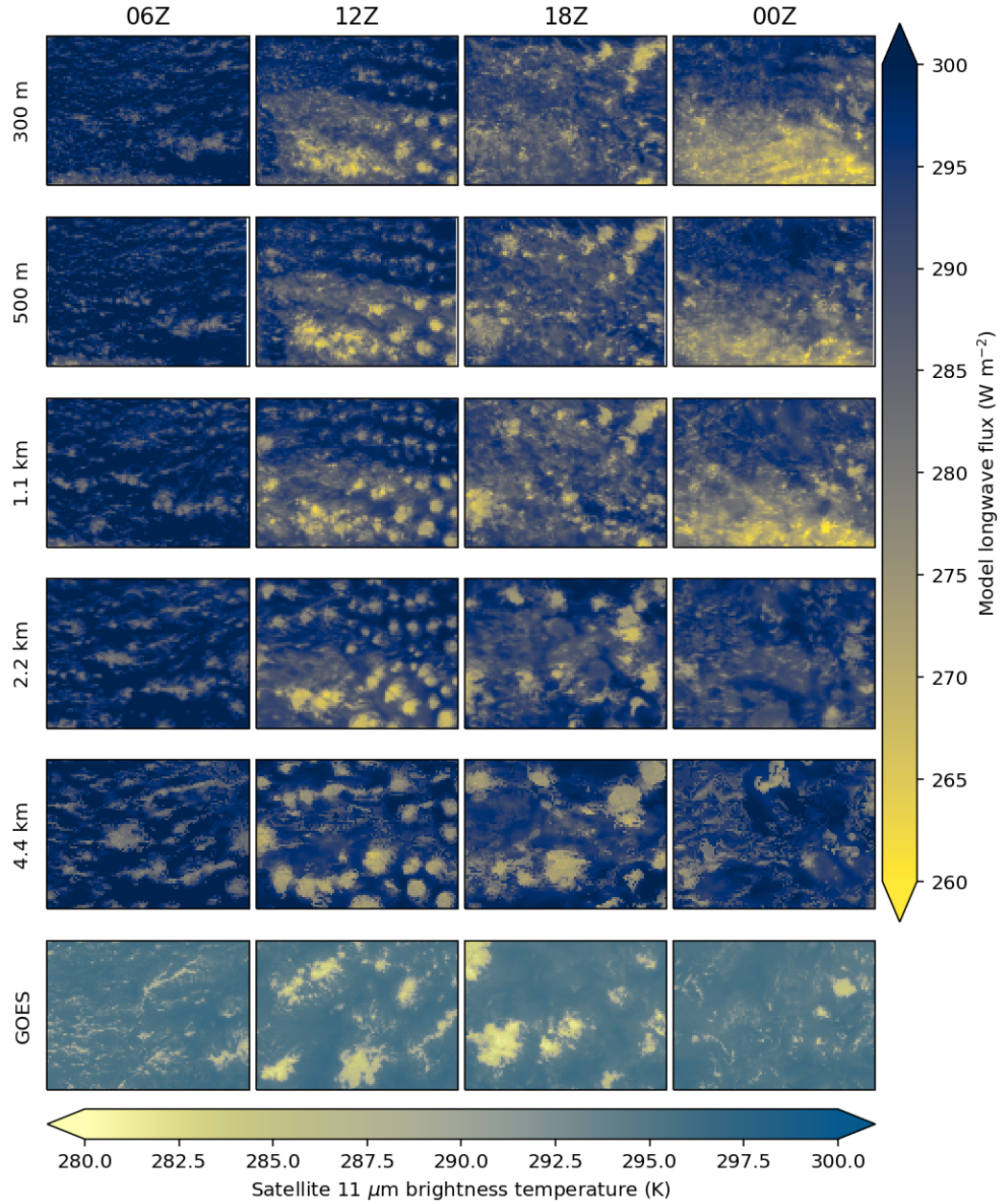
these two fields will not be exactly the same, they will capture a lot of the same features. Model data processed with a satellite simulator to mimic the brightness temperature from channel 11 does show that the following conclusions are consistent (see Appendix A).

Visually, all the simulations produce somewhat similar transitions in the cloud organization to those seen in the observations: initially small scattered clouds with some hints of lines (06Z) aggregate and develop into larger, more circular, cloud patches (12Z-18Z) followed by less aggregation and more cloud free air (00Z). In the terminology of Stevens et al. (2020), there is sugar at 06Z developing into flowers at 12Z and 18Z followed by sugar again at 00Z.

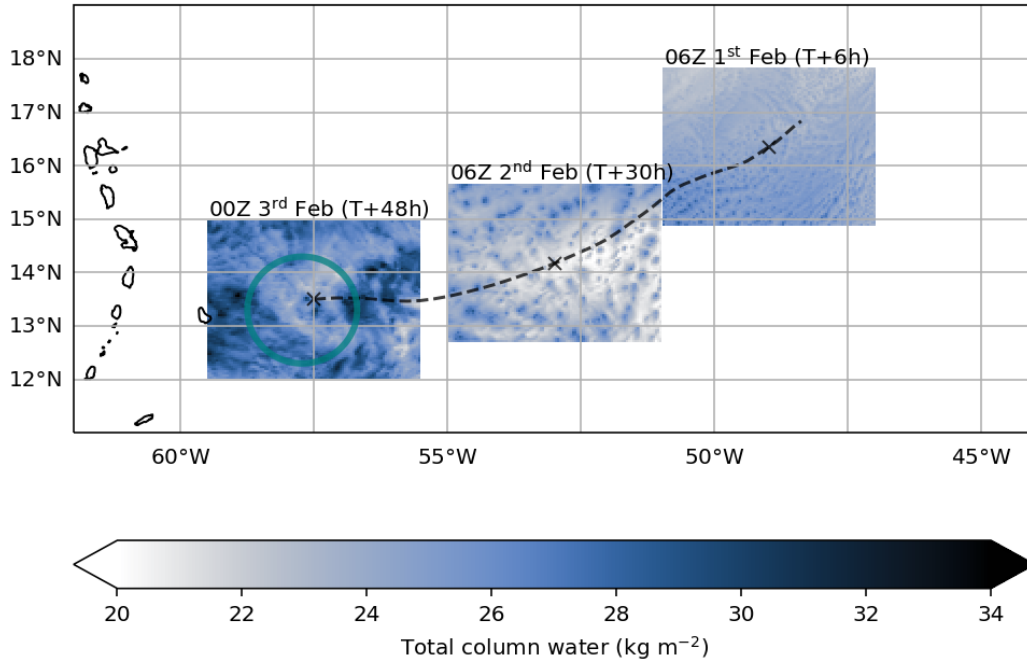
While we are interested in the development of mesoscale organization in the UM in this study, it is worth pointing out that these simulations have some strong differences compared to the observations (which are consistent in the simulated satellite imagery in Appendix A). The UM simulations produce too much cloud (too little cloud-free air) at all times. The satellite observations show there to be linear features as early as 00Z, before the flowers develop, most notably the structure in the top half of the domain near the center, but also weaker features in other parts of the domain. The UM does show some line-like structures, but at higher resolution they are fairly indistinct from the excessive amounts of scattered low clouds and at the lower resolution they are too large, and while there are more regions of clear air at lower resolution, they still cover too much of the domain. Similar resolution sensitivity is seen as the flowers develop (12Z-18Z): the 4.4 km simulation roughly captures the size of the flower structures but there are too many, too close together. At increasing resolution, the flowers are more broken up and there are too many small/low clouds in between.

### 3.1 Quasi-Lagrangian Domains

The fixed domain in Fig. 2 is limiting because we are not following the air mass as it develops and the air flowing into the domain has a strong influence on the cloud organization seen. This can be seen by the fact that the nested, inner-domain, simulations have very similar cloud structures to the driving 1.1 km simulation in Fig. 2. In the following sections, we will focus our analysis on what we call “quasi-Lagrangian domains” to better follow the development of the clouds.



**Figure 2.** Outgoing longwave flux from the UM simulations of 2<sup>nd</sup> February 2020. Each row shows a different resolution and each column a different time of day. Each simulation is shown re-gridded to the lowest resolution (4.4km) and to the area of the inner domain (red box in Fig. 1). The bottom row shows the  $11 \mu\text{m}$  brightness temperature from the GOES-16 geostationary satellite re-gridded to the same resolution (4.4 km) and area as the model data.



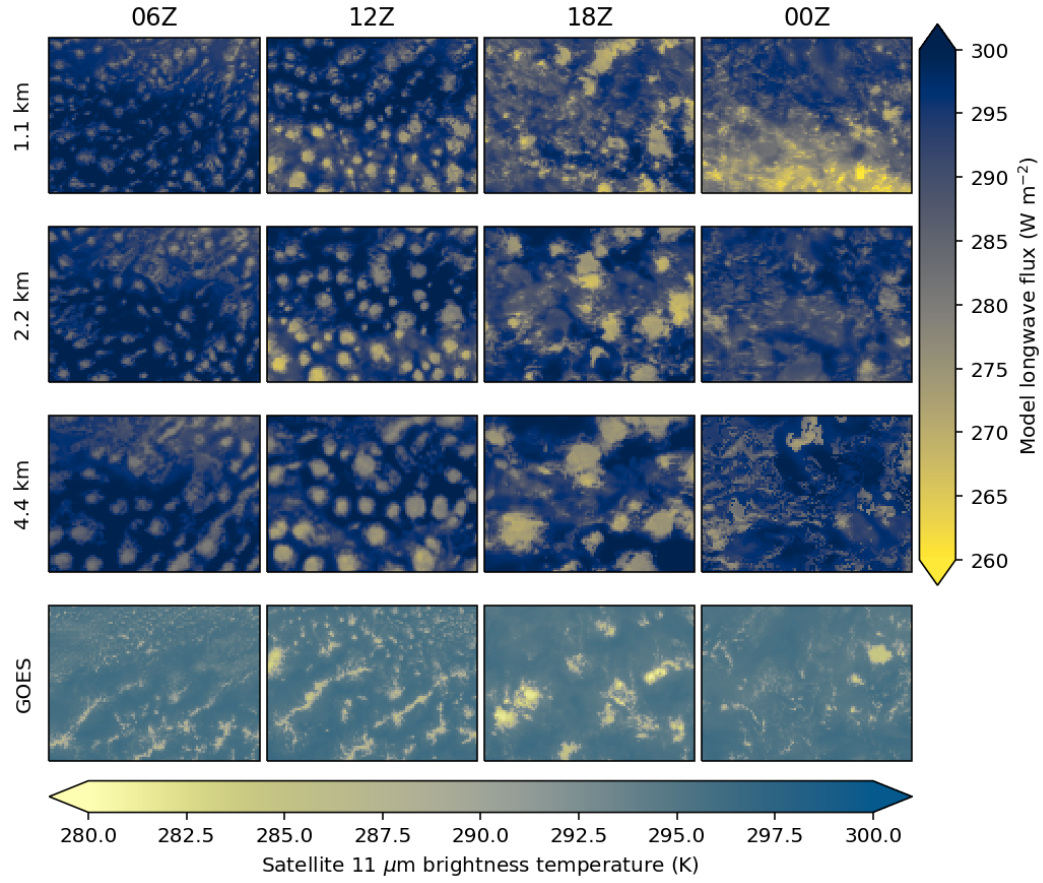
**Figure 3.** Quasi-Lagrangian domain extraction from kilometer-scale simulations. Shown is an example of extracting a quasi-Lagrangian domain following a trajectory from the 1.1 km simulation. The dashed line shows a back-trajectory from the center of the inner domain at the end of the simulation (T+48h/00Z 3<sup>rd</sup> February) and with a fixed height of 500m. The domain extracted is the same size as the inner domain but is translated to follow the trajectory. The three grids show snapshots of total column water for this subdomain extracted from the 1.1 km simulation.

Figure 3 shows an example of extracting a quasi-Lagrangian domain. A trajectory is calculated using Lagranto (Wernli & Davies, 1997; Sprenger & Wernli, 2015) with hourly wind output from the model and a fixed height of 500m (same height as Narenpitak et al. (2021)). The trajectory is initialized at 57.5W, 13.5N (the center of the inner domain) at the end of the simulation (T+48h/00Z 3<sup>rd</sup> February) and tracked back to the start of the simulation. The subset of the domain extracted is taken to be the same size as the inner domain. At T+48h, the domain is just the subset of the kilometer-scale domain that overlaps with the inner domain. At other times the location of this domain is translated to follow the trajectory and data linearly interpolated to the new grid. The dashed line in Fig. 3 shows the trajectory and extracted data for the 1.1 km simulation of 2<sup>nd</sup> February.

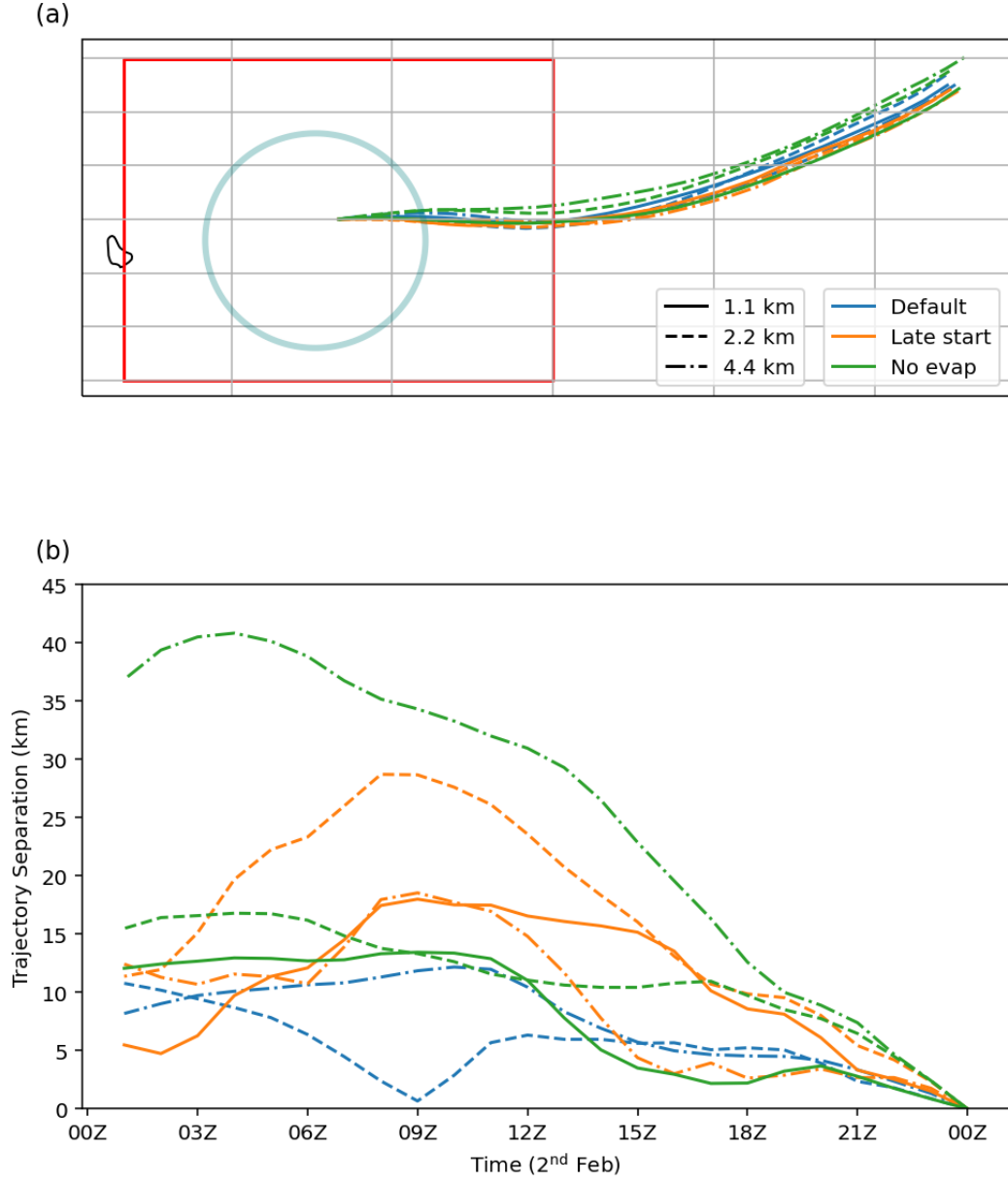
The method is similar to how Tomassini et al. (2017) extracted averages in a box following a model trajectory to compare with LES driven by forcings along the same trajectory. The quasi-Lagrangian domains are designed to be a rough equivalent of a Lagrangian LES, such as the simulations by Narenpitak et al. (2021) of the 2<sup>nd</sup> February case study. A key first test for the quasi-Lagrangian domain is that the developing cloud features remain within the domain to show we are tracking a coherent patch of cloud development. Animations of the model data on the quasi-Lagrangian domains does show most cloud features rotating around, but remaining within, the domain (not shown). In situations where wind shear or divergence had a stronger impact on displacing the cloud features from the feeding boundary-layer airmass this quasi-Lagrangian domain approach may not work and we would need a more sophisticated approach to track the boundaries of the cloud development.

Figure 4 shows the same satellite comparison as Fig. 2 but for the quasi-Lagrangian domains extracted from the kilometer-scale simulations. For the satellite data, we have interpolated it to the quasi-Lagrangian grid of the 4.4 km simulation. The specific choice of the 4.4 km quasi-Lagrangian grid makes very little difference to the figure. Figure 5 shows the trajectories used for extracting quasi-Lagrangian domains from simulations with different resolutions (and sensitivity tests used in later sections in this paper) and shows that the displacement between different trajectories is much smaller than the size of the domain. Another potential issue is that the trajectories from the simulations may differ from the true trajectories of the atmosphere; however, animations of the satellite data on the quasi-Lagrangian domains also show most cloud features remaining within the domain (not shown) indicating that we are also following the motion of the observed clouds with these trajectories.

The Lagrangian view in Fig. 4 is useful because it allows us to see the cloud development following the clouds, even in the observations. We see from the satellite data that the airmass that ends in the region of the inner domain has the clouds develop later: the developing line-like cloud patterns are still present in the upstream airmass at 12Z (Fig. 4) whereas there are already flowers present in the region of the inner domain at this time (Fig. 2). This means that if we were to only look at the clouds at a fixed position we would underestimate how rapidly the flowers develop and decay.



**Figure 4.** Same as Fig. 2 but for the quasi-Lagrangian domains extracted from the kilometer-scale simulations.



**Figure 5.** Trajectories used for extracting Lagrangian domains from kilometer-scale simulations. (a) Trajectories with the inner domain boundary (red) and HALO circle (teal) shown for context. (b) Distance between trajectories and the trajectory for the 1.1 km simulation initialized at 00Z 1<sup>st</sup> February. Orange lines are shown for the set of simulations initialized a day later (00Z 2<sup>nd</sup> February) and green lines are shown for simulations with evaporation of rainfall switched off.

Compared with the fixed domain evaluation in Fig. 2, the UM does much worse at getting the earlier development of the clouds upstream: at 06Z and 12Z the satellite shows line-like cloud features that intensify during this time whereas the UM produces mostly circular patches of cloud. There is a strong resolution dependence in the development of these cloud patches where lower resolution relates to larger cloud patches. This resolution dependence also affects the development of the flowers at 18Z, with the lower resolution producing larger flowers such that the flowers in the higher resolution simulations look most similar to the satellite, the opposite of what is seen at the region of the inner domain in Fig. 2. Nevertheless, the simulations do still produce a transition in cloud organization similar to that observed even if the clouds themselves look unrealistic.

### 3.2 Mesoscale organization

In this section we quantify the variation of mesoscale organization in the UM simulations in terms of horizontal variations in total column water. In Bretherton and Blossey (2017) and Narenpitak et al. (2021) the transition to mesoscale organization is seen by the emergence of mesoscale anomalies in total column water where mesoscale anomalies are defined as anomalies relative to the large-scale (domain) mean over 16x16 km horizontal blocks. Cumulus-scale anomalies are then defined as the anomalies at the grid-scale relative to the mesoscale anomalies such that a quantity, such as the total water content ( $q_t$ ), could be decomposed as

$$q_t(x, y) = \overline{q_t} + q_t''(x, y) + q_t'''(x, y), \quad (1)$$

where  $\overline{q_t}$  is the large-scale mean,  $q_t''$  is the mesoscale anomaly and  $q_t'''$  is the cumulus-scale anomaly. We use the same partitioning here, but use 17.6 km boxes for mesoscale anomalies because it is a factor of 4x relative to the coarsest resolution UM simulations (4.4 km). For the large-scale mean, we use the domain mean of the quasi-Lagrangian domain (i.e. the same size as the inner domain in Fig. 1).

Figure 6a show the mesoscale total column water (large-scale mean plus mesoscale anomaly) averaged over quartiles for the quasi-Lagrangian domains. All the simulations show a similar behavior with a weak decrease in total column water initially followed by a strong increase and finally decreasing or leveling out. Although all quartiles follow the same pattern, the magnitude of changes are not the same. Figure 6b shows the differ-

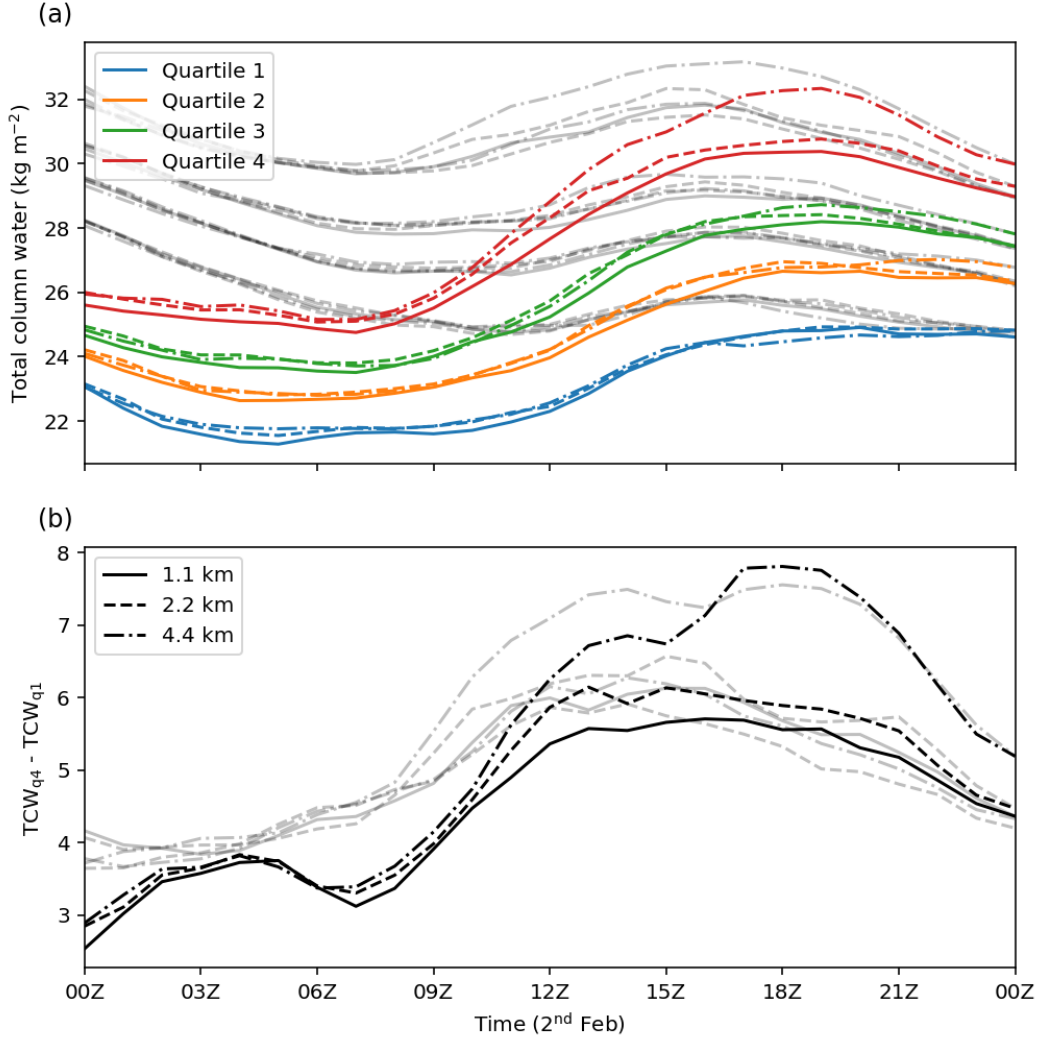


**Figure 6.** Mesoscale (17.6km) total column water as function of time in the quasi-Lagrangian subdomains extracted from kilometer-scale UM simulations. (a) Average over each quartile. (b) Difference between the moistest and driest quartiles. The gray-lines show the same quantities but for the spatially fixed inner subdomain (red box in Fig. 1).

ence between the average total column water for the moistest and driest quartiles which indicates the strength of the mesoscale organization. The mesoscale organization strongly increases during the initial development of the flowers from around 07Z-12Z and levels out before dropping off from 19Z as the flowers dissipate.

The gray lines in Fig. 6 shows the same averages but calculated fixed on the region of the inner domain. This demonstrates the added value of viewing the cloud development from a quasi-Lagrangian perspective. The region of the inner domain largely shows

a steady increase in mesoscale organization from the start of the day before leveling out and then decreasing; however, following the cloud development shows that the increase in mesoscale organization is stronger and faster, consistent with the differences seen between Figs. 2 and 4.

The strength of the mesoscale organization is stronger with lower resolution. This is particularly noticeable for the 4.4 km simulation which also has a second period where the mesoscale organization increases at around 15Z. This is consistent with seeing larger flower structures with lower resolution in the satellite comparisons (Figs. 2 and 4).

The increase in mesoscale organization during the development of the flowers is in agreement with Narenpitak et al. (2021); however, the timing and magnitude are very different. In Fig. 3 of Narenpitak et al. (2021) there is no initial contrast in total column water, only starting to develop after 14Z and continuing to increase into the following day. In our simulations the contrast in total column water prior to the development of the flowers is about as strong as at the end of the simulations in Narenpitak et al. (2021) and is decreasing by the end of the day. This can only partly be explained by the different domain. Using the same trajectory origin and (smaller) domain size as Narenpitak et al. (2021) gives us a quasi-Lagrangian domain that is roughly a subsection in the top right of the quasi-Lagrangian domains in Fig. 4 (not shown). The contrast in total column water between quartiles is smaller for this domain but still much stronger than in Narenpitak et al. (2021) and the timing is still the same (not shown). Instead, it looks like the UM simulations have a better representation of the mesoscale organization: in Fig. 2 of Narenpitak et al. (2021) the satellite shows more structure at the start of the simulation and develops a flower structure earlier and stronger than the LES, whereas the UM simulations develop the flower structures at a similar time to the satellite observations. These differences could be a spin up issue, which we investigate in section 3.4.

### 3.3 Processes Generating Mesoscale organization

In this section we look at the processes responsible for generating mesoscale organization in the UM simulations. Since mesoscale organization can be described as the development of moist and dry regions, Bretherton and Blossey (2017) derived a budget for the mesoscale anomalies of total water content,  $q''_t$ , and showed that it could be understood as the combination of two processes: 1) the advection of mesoscale anomalies of

moisture and 2) the “column process” described by Bretherton and Blossey (2017) as “the combined moistening effect of the moist processes and diabatically induced vertical advection across the horizontal-mean moisture gradient”. The equation is

$$\frac{\partial q_t''}{\partial t} = A_m + C_m \quad (2)$$

where

$$A_m = -(\bar{\mathbf{u}} + \mathbf{u}'') \cdot \nabla q_t'', \quad (3)$$

where  $\mathbf{u}$  is the 3d wind, and

$$C_m = \frac{1}{\rho_0} \frac{\partial}{\partial z} [P - F_{qt}^{cu}]_m - w'' \frac{d\bar{q}_t}{dz}, \quad (4)$$

where the terms in eq. 4 can be described in three parts (as in Narenpitak et al. (2021)). The first term,  $P$ , represents the non-advective fluxes of moisture from precipitation and surface fluxes, and the  $[\cdot]_m$  denotes a mesoscale average. The second term,  $F_{qt}^{cu}$ , represents the cumulus-scale fluxes of moisture. Narenpitak et al. (2021) included the vertical ( $B_v$ ) and horizontal ( $B_h$ ) cumulus-scale fluxes, where

$$B_v = \frac{1}{\rho} \frac{\partial}{\partial z} [\rho w''' q_t''']_m, \quad (5)$$

$$B_h = -\nabla_h \cdot [\mathbf{v}''' q_t''']_m, \quad (6)$$

where  $w$  and  $\mathbf{v}$  are the vertical and horizontal winds respectively. The inclusion of the horizontal fluxes by Narenpitak et al. (2021) is because, unlike (Bretherton & Blossey, 2017), they did not to apply a scale separation to simplify these terms. See appendix D of Narenpitak et al. (2021) for full details. The final term,

$$C = -w'' \frac{\partial \bar{q}_t}{\partial z}, \quad (7)$$

is the vertical advection of large-scale moisture by the mesoscale winds and was shown to be the dominant term in the column process by Narenpitak et al. (2021).

We have calculated each of these terms for the quasi-Lagrangian domains. Figures 7 and 8 show each of these terms, except the non-advective fluxes, as vertical profiles at 10Z (i.e. when the mesoscale aggregation is rapidly increasing) and vertically integrated as a function of time respectively. Only the 1.1 km and 4.4 km are shown for clarity since the 2.2 km simulation falls between the two.

Consistent with Bretherton and Blossey (2017) and Narenpitak et al. (2021), the vertical advection of large-scale moisture by the mesoscale winds,  $C$ , is the most impor-

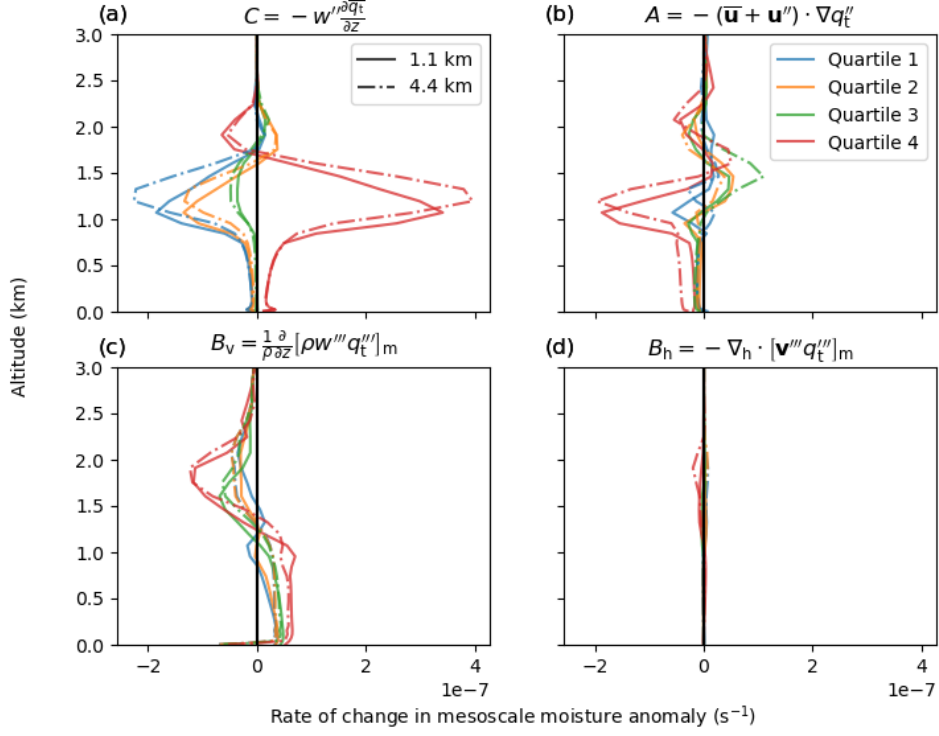


**Figure 7.** Profiles of terms affecting mesoscale moisture anomalies, calculated following Narenpitak et al. (2021), for the Lagrangian subdomains extracted from kilometer-scale simulations at 10Z 2<sup>nd</sup> February (T+34h). (a) Advection of large-scale moisture by mesoscale vertical velocity (b) Advection of mesoscale anomalies of moisture. (c) Vertical cumulus-scale moisture fluxes. (d) Horizontal cumulus-scale moisture fluxes.

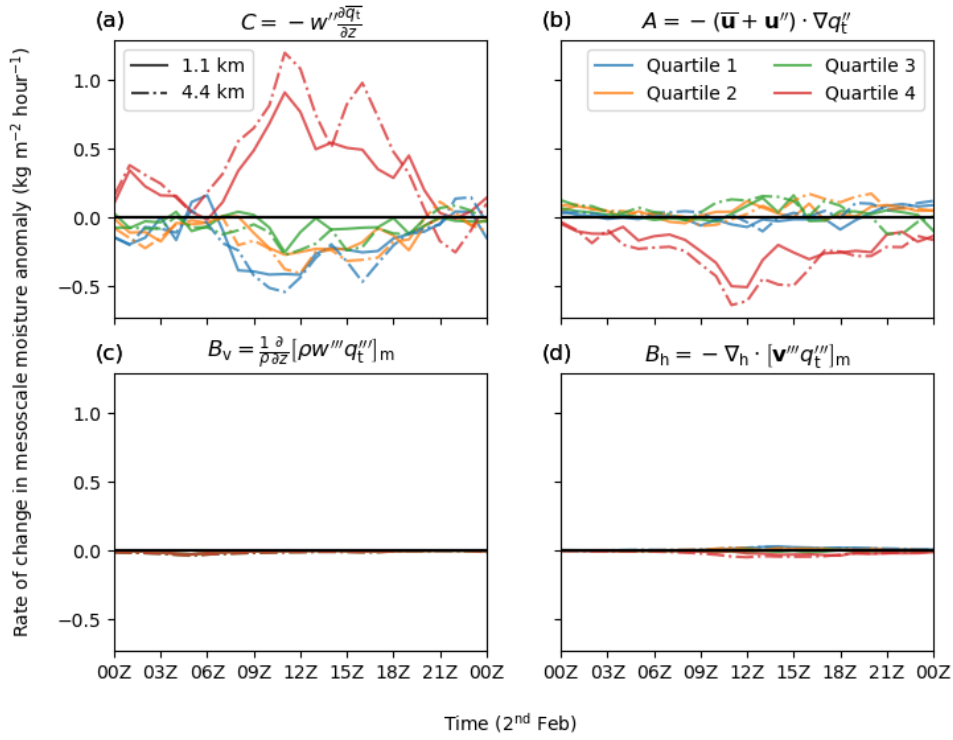


**Figure 8.** Column averages of terms in Fig. 7 at all times on 2<sup>nd</sup> February. (a) Advection of large-scale moisture by mesoscale vertical velocity (b) Advection of mesoscale anomalies of moisture. (c) Vertical cumulus-scale moisture fluxes. (d) Horizontal cumulus-scale moisture fluxes.

tant process for increasing aggregation. It is responsible for moistening the moistest regions and drying in other regions. The advection of mesoscale anomalies,  $A$ , also acts to oppose the aggregation by removing moisture from the moistest regions but is weaker than  $C$  during the middle of the day when we see aggregation increasing. The cumulus-scale fluxes ( $B_v$  and  $B_h$ ) have negligible contributions to the column averages.

To quantify the effect of the non-advective fluxes ( $P$ ) on mesoscale organization, we use hourly accumulated rainfall and a tracer that accounts for the net effect of surface evaporation. The tracer for surface evaporation comes from a set of moisture tracers designed to represent a Lagrangian budget of specific humidity, where the rate of change of specific humidity ( $q$ ) is

$$\frac{Dq}{Dt} = \sum_i \frac{dq_i}{dt}, \quad (8)$$

where the sum over  $i$  represents all the non-advective processes modifying the specific humidity of an air parcel in the UM. The total specific humidity is then given by

$$q = q(t = t_0) + \int_{t_0}^{t_0 + \Delta t} \frac{Dq}{Dt} dt = q_{adv} + \sum_i q_i, \quad (9)$$

where each  $q_i$  is represented by an individual tracer that accumulates the changes from a single process in the UM at each timestep and  $q_{adv}$  represents the initial field of specific humidity which is passively advected by the UM.

The tracers are initialized at 00Z 2<sup>nd</sup> February and then tracked until the end of the simulation. The distribution of the passive tracer ( $q_{adv}$ ) then tells us about how water vapor changes due to advection of the initial water vapor and the other tracers tell us about the net effect of individual sources and sinks of water vapor on air parcels. Most of the tracers account for changes between water vapor and other phases of water. The processes that affect the total water content are evaporation of water into the atmosphere from the surface and removal of water from the atmosphere by precipitation.

Evaporation of water from the surface is accounted for by the tracer which tracks changes from the boundary-layer parametrization. The boundary-layer parametrization only redistributes moisture vertically (Lock et al., 2000), so the increment to the tracer tells us about how subgrid-scale turbulent mixing redistributes moisture vertically. More relevant here, is that this tracer also accounts for surface fluxes of moisture, so the column average of a single timestep increment applied to this tracer tells us about the net effect of surface fluxes on column moisture. Since the tracer is advected following the

flow the effects of advection on column moisture could become more important in this tracer at later times if, for example, wind shear acts to separate evaporated moisture from the column of interest. This is not important over the short integration time in our simulations as the horizontal distribution of this tracer stays reasonably uniform.

To account for precipitation we just use the model output of hourly accumulated rainfall rather than a tracer. This has the disadvantage that the output precipitation is associated with where it fell rather than the air parcel that it fell from; however, we do see that most of the hourly accumulated rainfall is still associated with the moistest quartile so this is not a problem here.

Figure 9 shows the change from the previous output (i.e. rate of change per hour) of column-averaged quantities by quartile of total-column water. The aggregation can mostly be explained by the dynamics rather than direct effects of non-advective moisture fluxes (surface evaporation and rainfall) because the pattern of differences between the quartiles for specific humidity is mostly explained by the passive tracer ( $q_{adv}$ ). The boundary-layer fluxes largely just moisten all quartiles evenly with a small opposition to aggregation early on and small enhancement to aggregation later. The rainfall acts to oppose aggregation after it develops since it is dominated by removing moisture from the moistest quartile, but it is also small compared to the differences seen in the passive tracer. This small contribution of non-advective moisture fluxes to aggregation is consistent with Narenpitak et al. (2021).

Bretherton and Blossey (2017) found that the aggregation in their simulations slowed down when the advection of the mesoscale anomalies became strong enough, due to the mesoscale anomalies being stronger, to oppose the aggregation from the column process. However, in our simulations, the changes in aggregation largely follow the changes in the strength of moistening from mesoscale vertical velocities on the background moisture gradient ( $C$ ). The advection of mesoscale anomalies of moisture acts to oppose aggregation throughout the day, with a moderate increase when the strength of these anomalies increases, but it is  $C$  that varies more with a strong increase from 09Z-12Z which is associated with the increasing variance in total column water and a strong decrease toward the end of the day associated with the variance in total column water decreasing.

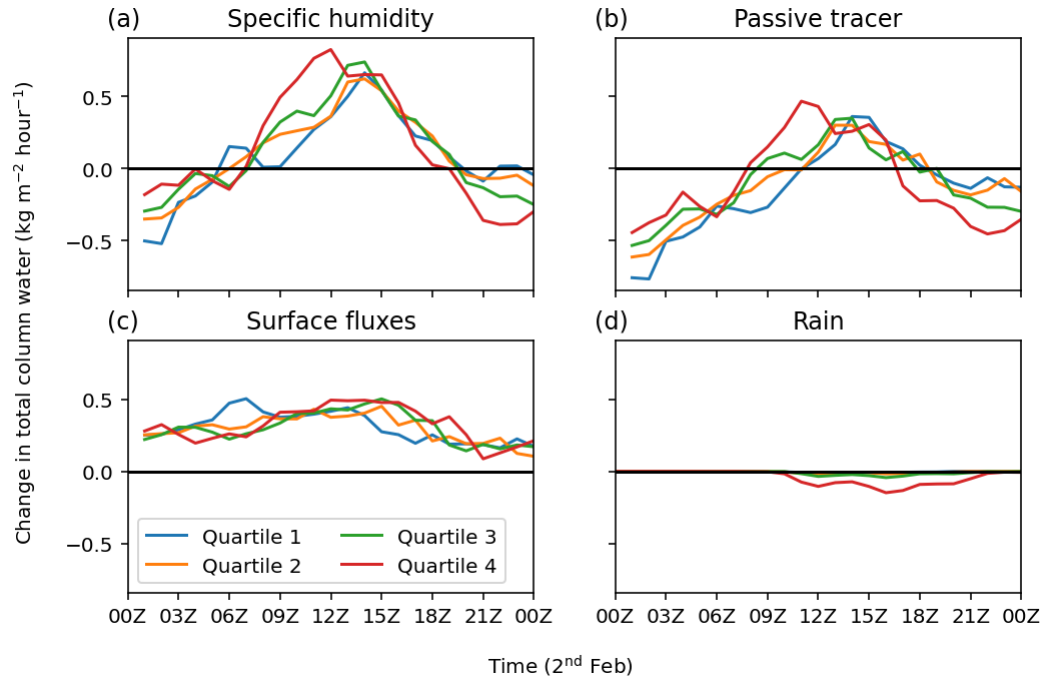


**Figure 9.** Change in column water over one hour due to different processes, averaged over quartiles of column water, for the 1.1 km quasi-Lagrangian domain. (a) Total column water. (b) Total column water from a passive tracer initialized at 00Z 2<sup>nd</sup> February. (c) Total column water from a tracer that tracks changes in moisture from the boundary-layer parametrization. (d) Accumulated rainfall.

### 3.4 Influence of Spin-up Time on Mesoscale organization

Our simulations have stronger and earlier development of mesoscale organization compared to the LES simulations of Narenpitak et al. (2021); however, the LES simulations of Narenpitak et al. (2021) do develop flowers later than the observations and also appear to be too uniform. This could be related to the different ways the simulations are spun up. Our simulations are initialized at 00 UTC 1<sup>st</sup> February by interpolating ERA5 data to the UM model grid, whereas the simulations of Narenpitak et al. (2021) are initialized at 02 UTC 2<sup>nd</sup> February using information from ERA5 at a single point on a trajectory. Therefore, our simulations have an extra 26 hours of spin up and also already include some horizontal variability from the ERA5 initial conditions. To test whether we could delay the development of mesoscale organization and flowers by having a less organized state in our simulations at the time when the flowers develop in the observations, we re-ran our simulations initialized 24 hours later (00Z 2<sup>nd</sup> February) so that the model has had less time to spin up any clouds and mesoscale structure from the ERA5 initial conditions.

Figure 10a shows outgoing longwave fluxes for these simulations with a later start time. The comparison is shown for quasi-Lagrangian domains in the same way as Fig. 4. The difference in trajectory location for the different start times, as with the different resolutions, is small compared to the size of the domain (see Fig. 5), so any differences seen are due to the simulation of the cloud development.

There are strong differences between the simulations at different start times in the cloud organization. The simulations initialized later have much smaller cloud structures. This makes sense because at earlier lead times the model is still spinning up cloud structures and is noticeably smoother at 06Z. The smaller cloud structures persist even as the later initialized model runs start to produce similar cloud structures at 12Z. This leads to the flower structures at 18Z being smaller and perhaps looking more like the cloud structures in the observations. Both sets of simulations look more similar at the end of the day when the flower structures have broken down.

Despite the differences in the cloud structures for the different initialization times, the general development of the clouds follows the same pattern, with little organization initially (06Z), followed by development into larger cloud structures (12Z-18Z) which are

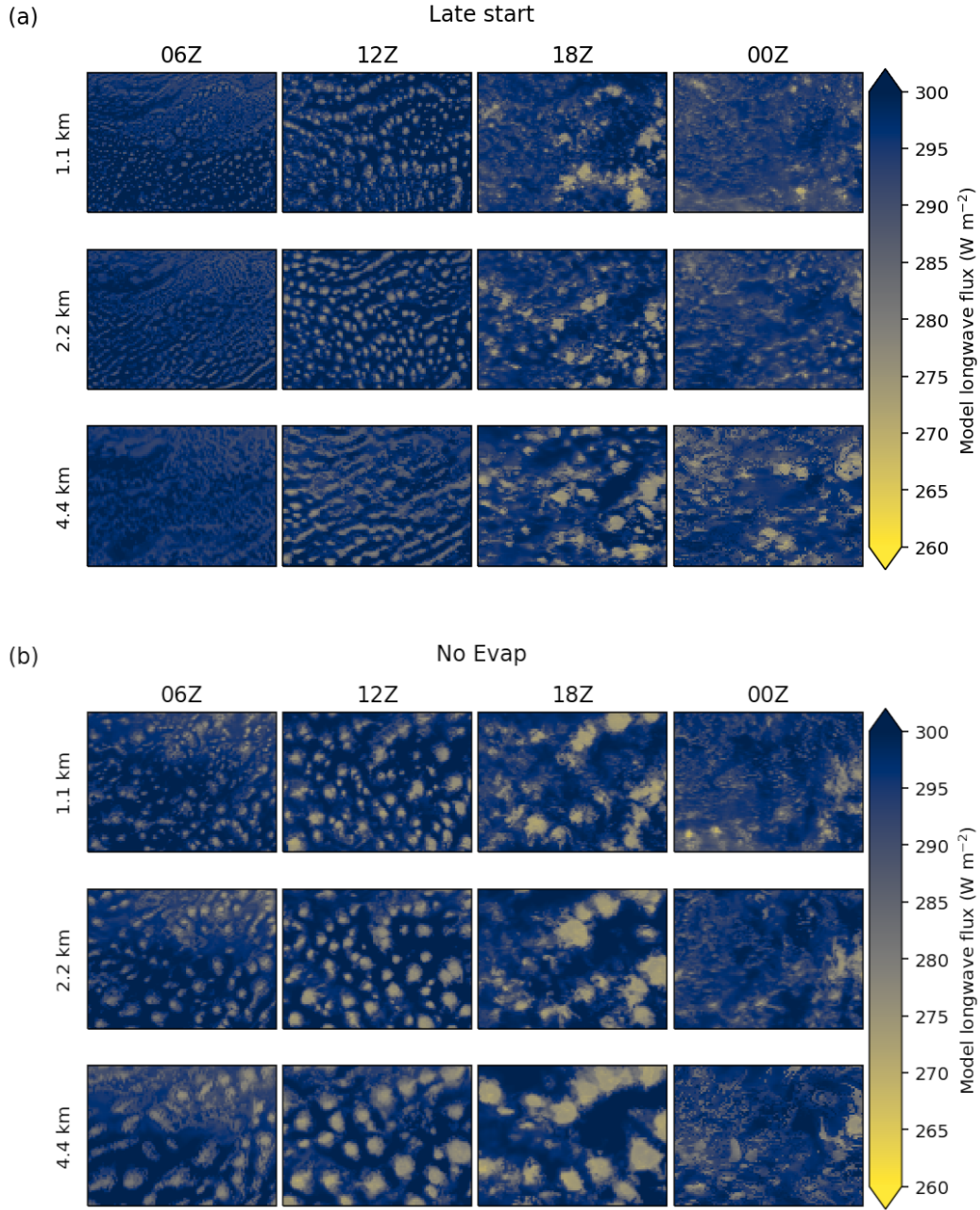


**Figure 10.** Outgoing longwave flux. Same as in Figs. 2 and 4 but for the quasi-Lagrangian domains extracted from (a) simulations initialized a day later (00Z 2<sup>nd</sup> February) and (b) simulations with no evaporation of rainfall.

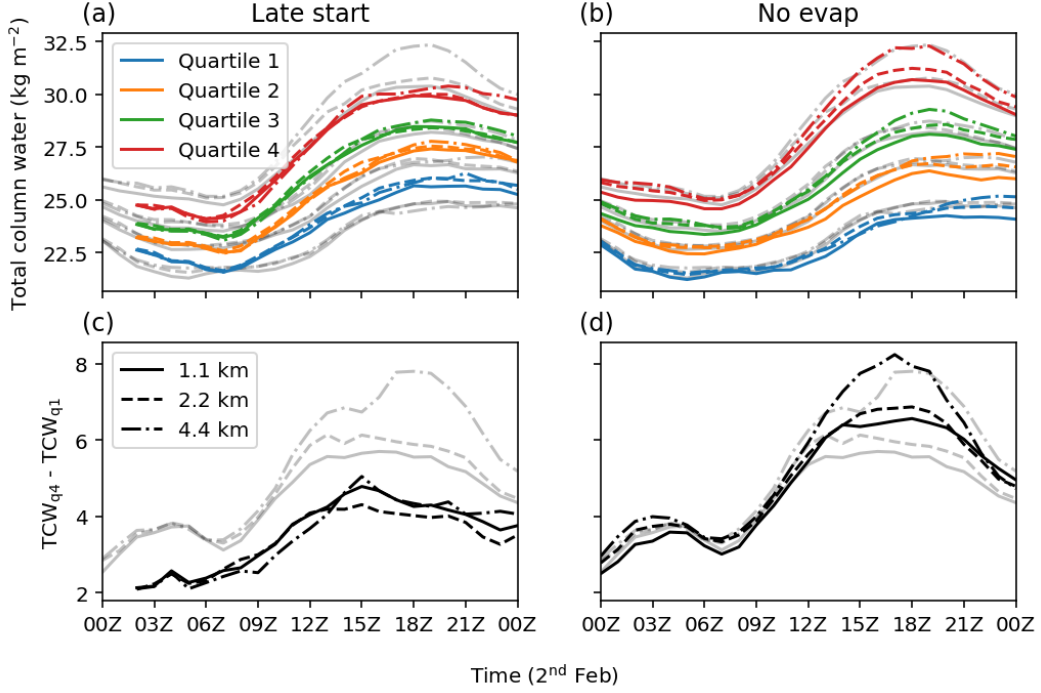


**Figure 11.** Same as Fig. 6 but for the quasi-Lagrangian domains extracted from (a)/(c) simulations initialized a day later (00Z 2<sup>nd</sup> February) and (b)/(d) simulations with no evaporation of rainfall. The gray lines shown in this figure are the colored lines from Fig. 6.

mostly gone by the end of the day (00Z), although the 4.4 km simulation does retain some larger cloud structures at this time.

This consistency in the cloud development can also be seen in the total column water. Figure 11a shows the mesoscale total column water averaged over quartiles for the quasi-Lagrangian domains from the simulations with a later start time. For comparison, the lines for the earlier start time simulations (from Fig. 6) are shown in gray. The strength of mesoscale organization (Fig. 11c) is always weaker in the simulations initialized later, but the timing of the increase is fairly similar. The distribution of total column water only converges towards the end of the day when the mesoscale organization decreases more rapidly in the simulations initialized earlier. The similarity in the timing of the development suggests that the development of the flowers are related to large-scale dynamics the effects of the diurnal cycle rather than some threshold reached in the cloud development. However, the initial development does have a strong effect on the details of the flower structures in these simulations.

### 3.5 Influence of Cold Pools on Mesoscale organization

In section 3.3 we showed that the mesoscale organization stops increasing because the effects of mesoscale vertical velocities, through the column process, decreases. One possible reason for decreasing strength in the column process is the development of cold pools. The flowers are associated with precipitation which develops cold pools in the moist regions because the clouds develop in the moist regions. If the cold pools sufficiently suppressed convection in these regions then the circulation making the moist regions moister would be stopped.

To identify cold pools in our simulation we use the tracer that accumulates changes in moisture due to the evaporation of rainfall in the microphysics parametrization (CASIM) from the tracers described in section 3.3. As with the tracers in section 3.3, the tracer is initialized at 00Z 2<sup>nd</sup> February. Figure 12 shows two snapshots of this tracer from the quasi-Lagrangian domain extracted from the 1.1 km simulation. Also shown is the equivalent potential temperature, which can also be used to identify cold pools. We see that at the earlier time (12Z) the tracer has a close correspondence to equivalent potential temperature where the cold pools are initially developing directly underneath the clouds. At the later time, the cold pool activity is less distinct in equivalent potential temperature, but the tracer shows that a large amount of the domain has been affected by cold pools over the course of the day.

To test whether the cold pools influence the mesoscale organization, we re-ran our simulations with evaporation of rain switched off, which stops the cold pools from forming. Figure 11b shows the mesoscale total column water averaged over quartiles for the quasi-Lagrangian domains from the simulations with no evaporation of rain and gray lines for the original simulations (from Fig. 6). As with the simulations with different resolutions and start times, the difference in trajectory location for the different the simulations with no evaporation of rain is small compared to the size of the domain (see Fig. 5), so any differences seen are due to the simulation of the cloud development.

The cold pools only have a small effect on the strength of mesoscale organization with the simulations with cold pools suppressed showing stronger development of mesoscale organization (Fig. 11d). The overall difference in mesoscale organization is small compared to the original simulations with the initial increase in mesoscale organization largely unaffected. The timing of the increase and decrease in mesoscale organization is simi-

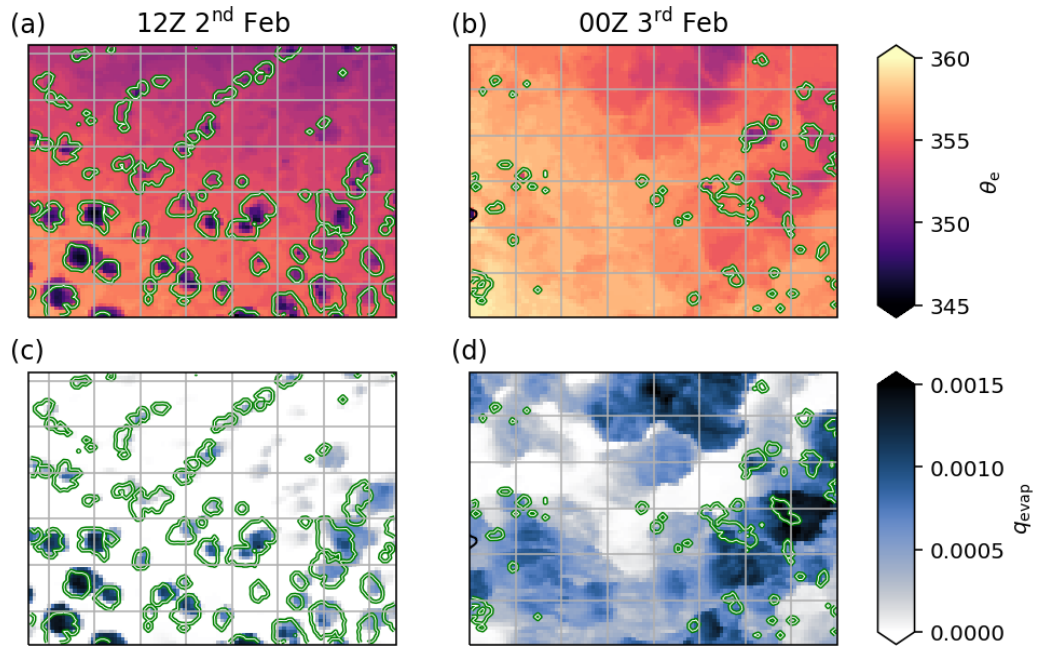


**Figure 12.** Snapshots of (a)/(b) equivalent potential temperature and (c)/(d) moisture tracer for evaporation of rainfall, on the lowest model level for the quasi-Lagrangian domain extracted from the 1.1 km simulation of 2<sup>nd</sup> February. The green/white lines show clouds at 2 km (liquid water > 0.01 g kg<sup>-1</sup>).

lar in all the simulations, indicating that the cold pools only modulate the mesoscale organization, rather than being the main process stopping further development.

The simulations with no evaporation having stronger mesoscale organization may indicate that the cold pools do act to suppress convection in the moistest regions. Comparing the outgoing longwave flux after the flowers have developed (Figs 4 and 10) we see that the simulations without cold pools are associated with slightly larger flower structures, most noticeable at higher resolution, indicating that the cold pools do have a small effect on the development of the flowers.

The outgoing longwave flux shows larger differences in the regions between the flowers where the simulations without cold pools have much less low cloud indicating that these clouds are primarily generated by the interactions of cold pools. The original simulations have too much of this low cloud compared to the satellite observations suggesting that the UM produces too many/too strong cold pools or too many clouds from the interactions of cold pools. We can say that the original UM simulations probably are producing too many cold pools because they produce too many cloud structures compared to satellite observations (Fig. 4) and each of these cloud structures is associated with precipitation and cold pools (Fig. 12).

The differences in moisture are not only in the moistest regions and the 4.4 km simulation actually has fairly similar total column water for the moistest quartile in the simulations with and without evaporation of rain. Another difference is that the other quartiles are drier in the simulations with no evaporation of rain at the time when the cold pools are initially developing in the reference simulation. This could be due to the cold pools acting to transport moisture from moister region to drier regions, which would make sense, although it could also just be a sign of weaker convergence of moisture to the moistest regions.

### 3.6 Domain Averages

In the previous sections, we showed that the initial organization and cold pools both have little effect on the timing of the development of mesoscale organization and flowers. This indicates that it is the large-scale circulation that is driving the development of the flowers. To compare differences in the large-scale circulation between simulations, we have computed domain averages for the quasi-Lagrangian domains extracted from

the kilometer-scale simulations, including the sensitivity tests from sections 3.4 and 3.5. The domain averages, shown in Fig. 13, can also tell us about the impacts of the flows on the large scale.

The total column water is similar across all the simulations, although there is a tendency for higher resolution to be drier, showing that the mean total column water is a poor predictor of the clouds and organization. The development of the flowers and increase in mesoscale organization is associated with the time when the large-scale total-column water is increasing. This is related to the large-scale vertical velocity changing from negative to positive (Fig. 13b), indicating large-scale convergence of moisture. This is consistent with (Narenpitak et al., 2021) who showed the development of flowers was associated with positive large-scale vertical velocity and a weaker vertical velocity resulted in slower development of mesoscale organization; however, it is difficult to determine cause and effect from our simulations and the large-scale moisture convergence could be a result of the development of the flowers.

In contrast to total column water, the liquid water is strongly dependent on resolution. The differences in liquid water make sense since we see differences in the cloud structures. Higher resolution is associated with less liquid water which makes sense since we have seen that higher resolution is also associated with smaller cloud structures. Despite the sensitivity to resolution of liquid water, the sensitivity of precipitation to resolution is less obvious. While there can be large differences in total precipitation between simulations, there is no obvious link to resolution. This implies that the differences in liquid water are not linked to the clouds that form precipitation or there are compensating changes in the intensity of precipitation. Instead the differences are only associated with the difference size cloud structures. There are differences in precipitation associated with start time with the simulations that are initialized later developing precipitation later and producing less precipitation overall which makes sense since these simulations start with, and develop, smaller cloud structures. Unsurprisingly, the simulations without evaporation of rainfall have more precipitation since the precipitation all falls to the ground rather than forming cold pools. The simulations without evaporation of rainfall also show more liquid water after the initial development which makes sense because there are no cold pools to suppress further development of the clouds. However, the difference in liquid water large compared to what would be expected from looking at the differences in the cloud structures.

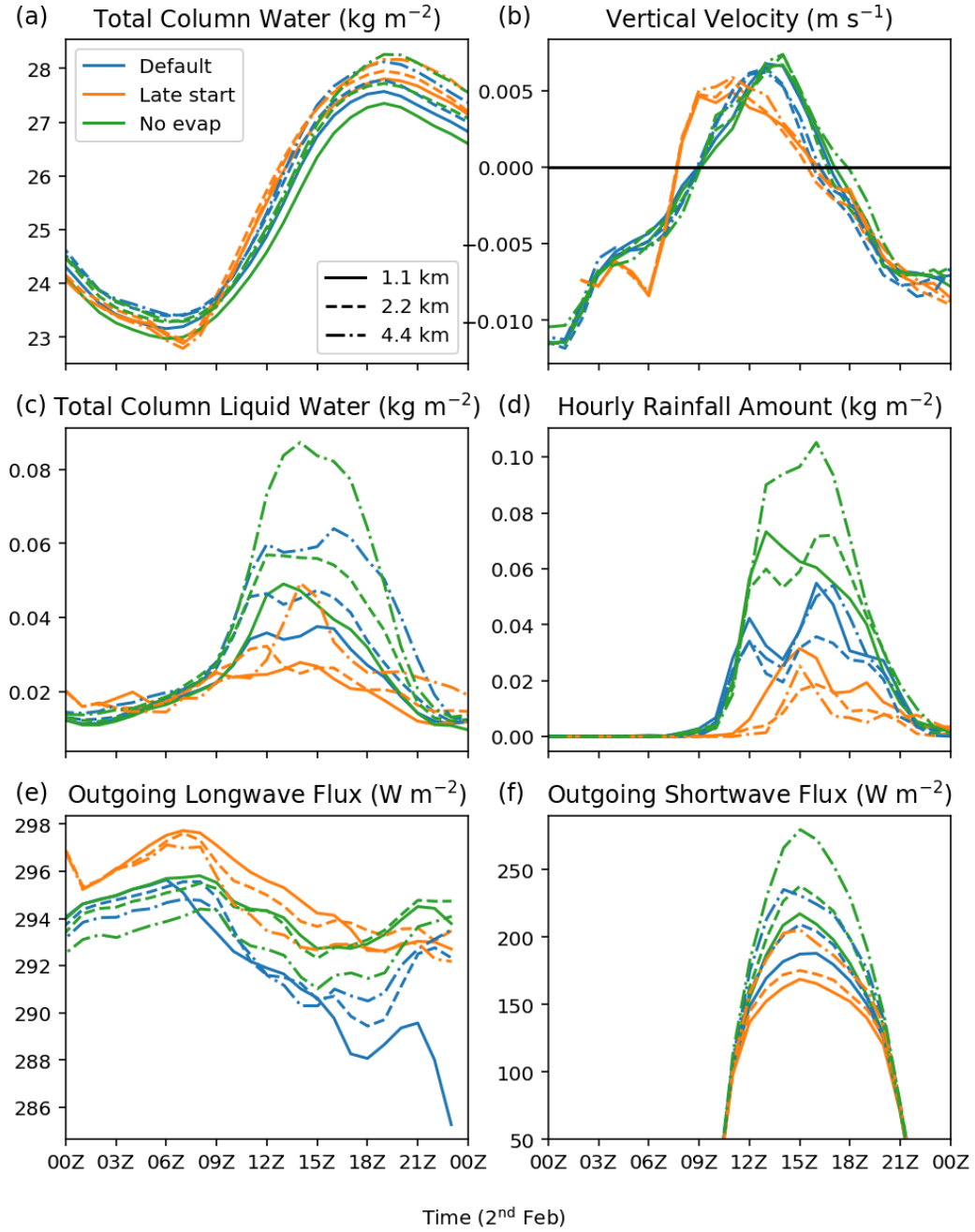


**Figure 13.** Domain means of quasi-Lagrangian domains extracted from kilometer scale simulations for the reference simulations (blue), simulations initialized a day later (00Z 2<sup>nd</sup> February in orange), and simulations with evaporation of rainfall switched off (green). (a) Total column water. (b) Vertical velocity averaged from 0-2 km. (c) Total column liquid water. (d) Hourly accumulated rainfall. (e) Outgoing longwave flux. (f) Outgoing shortwave flux.

As expected, the differences in cloud structures are associated with differences in radiation. The average outgoing longwave flux is most sensitive to the spin up. This makes sense when looking at Figs. 4 and 10 because the simulations with the earlier start time have larger cloud structures and therefore a lower domain-average outgoing longwave flux. We would expect to also see a strong sensitivity to resolution for the same reason, lower resolution has larger cloud structures, but there is some compensation where the lower resolution simulations also have less low cloud cover giving a similar average. This compensation is stronger in the simulations initialized earlier as the resolution sensitivity is still apparent for the later start time simulations at the middle of the day. The simulations with no evaporation of rainfall also show differences in outgoing longwave radiation largely due to there being less low cloud once the flowers develop. There are also smaller differences in the outgoing longwave flux prior to the development of the flowers which will be due to small differences in the simulation of the initial 24 hours.

In contrast to the outgoing longwave flux, the outgoing shortwave flux is much more strongly sensitive to resolution, as well as the initial structures and the cold pools. This is because the outgoing shortwave flux is less dependent on the low cloud, so it provides less of a cancellation to the sensitivity to the size of the cloud structures.

## 4 Conclusions

We have run high-resolution simulations of the 2<sup>nd</sup> February case study from EUREC<sup>4</sup>A with the Met Office’s unified model (UM). This case study is of interest because the cloud organization transitions from a regime of shallow, disorganized, cumulus clouds, known as “sugar”, to a regime of deeper clouds with large detrainment layers, known as “flowers”. The UM simulations reproduce the observed increase in mesoscale organization associated with the development of the flowers; however, the details of the clouds have some issues: the UM produces too much shallow cloud and the size of the deeper cloud structures are sensitive to resolution, with lower resolution producing larger cloud structures.

To better follow cloud development, we focused our analysis on subdomains extracted from our simulations following boundary-layer trajectories. These “quasi-Lagrangian” domains allow us to focus our analysis on the development of organization following the clouds. The main motivation behind using these quasi-Lagrangian domains was to compare our results with the Lagrangian LES results from Narenpitak et al. (2021) where

the LES is driven by forcings following a trajectory. Higher resolution nested simulations provided little extra value to compare with Lagrangian LES because of the limited domain size making them too dependent on the simulation which supplied the boundary conditions.

Consistent with Narenpitak et al. (2021), we find that the development of the flowers is associated with an increase in mesoscale organization generated by the mesoscale vertical velocities and associated moisture transport. This process, first described by Bretherton and Blossey (2017), is where latent-heating driven mesoscale vertical velocities provide a positive feedback on convection by converging moisture towards the convection, making moist patches moister and dry patches drier. It is useful that we have shown that the kilometer-scale UM simulations can reproduce this process because that means these simulations can be used to better understand the sensitivity of mesoscale organization to changes at larger scales.

We found that our simulations differed from the LES of Narenpitak et al. (2021) in the timing and the magnitude of the development of mesoscale organization. In the simulations of Narenpitak et al. (2021), the mesoscale organization develops from an initially horizontally homogenous state (zero mesoscale organization) and continues to increase past the end of the day, whereas in our simulations, there is already mesoscale organization present and the development of the flowers is associated with an approximate doubling in the strength of the mesoscale organization. We also find that the development of mesoscale organization is more rapid in our simulations and starts to decrease by the end of the day. The development of mesoscale organization in our simulations does appear to be more consistent with satellite observations.

To test whether the initial organization we see in our simulations strongly impacted the development of the flowers, we re-ran our simulations initialized one day later (00Z 2<sup>nd</sup> February) to have a less organized state on 2<sup>nd</sup> February. We found that the timing of the development of mesoscale organization and the flowers was unchanged despite the mesoscale organization always being weaker, and the cloud structures being smaller, in the simulations with a later start time.

In the simulations of Bretherton and Blossey (2017), they found that the development of mesoscale organization stopped once the mesoscale anomalies became strong enough that the dis-aggregating effect of advection on the mesoscale anomalies balanced the ag-

gregating effect of the circulation generated by the effect of mesoscale vertical velocities on the background humidity profile. In our simulations, the two processes do not reach a balance, instead the decrease in aggregation happens when the aggregating effect of the mesoscale vertical velocities strongly decreases.

A possible explanation for why the aggregation stops increasing is that cold pools generated from evaporation of rainfall underneath the flowers act to suppress convection in the moistest regions, stopping the circulation from converging more moisture to these regions. However, sensitivity studies with evaporation of rainfall switched off showed that the effect of cold pools on mesoscale organization is weak. The cold pools do still have important effects on radiation by generating low clouds in the regions between the flowers; however, these clouds are over represented in our simulations.

The lack of sensitivity in the timing of the development and decay of the flowers to initial organization and cold pools in our simulations indicate that the development of mesoscale organization is instead driven by the large-scale circulation. The development of mesoscale organization in our simulations is associated with large-scale moisture convergence. It is difficult to determine cause and effect from our simulations and the large-scale moisture convergence could just be signature of the development of the flowers. This result is consistent with Narenpitak et al. (2021), who showed that the development of flowers was associated with the forcing of positive large-scale vertical velocity and a weaker forcing resulted in a slower development of mesoscale organization.

A limitation in the kilometer-scale simulations here is that they do exhibit strong sensitivities to resolution. Larger flower structures are associated with lower resolution. This sensitivity is seen in shortwave radiation, because the larger flowers reflect more shortwave radiation. However, the sensitivity is less obvious in longwave radiation, due to compensating decreases in low cloud in the simulations with larger flowers. This presents a problem for kilometer-scale climate projections because the sensitivity of radiative fluxes to changes in mesoscale organization will still be uncertain. The poor representation of the cloud structures compared to observations would not be fixed by tuning the radiative fluxes because the changes in radiation, not just the absolute values, are sensitive to the model setup.

Given the large problems and sensitivities of these kilometer-scale models in producing trade-wind cumulus and the associated radiation, they cannot be considered as

a solution for uncertainties in climate sensitivity yet. There is still more work needed on the representation of mesoscale organization and clouds in models at this scale. However, given the models reproduce the variations in mesoscale organization and associated processes, they are a useful tool for understanding processes driving mesoscale organization and interactions with larger scales.

## Appendix A Simulated Satellite Observations

Figure A1 shows 11  $\mu\text{m}$  brightness temperature from the UM simulations and the GOES-16 satellite. The brightness temperature from the UM simulations is produced using the satellite simulator RTTOV (Saunders et al., 2018). The important point here is that the simulated satellite comparison agrees with the conclusions drawn from looking at outgoing longwave flux in Fig. 2: i) the model simulations produce too much cloud (not enough clear sky), ii) lower resolution is associated with larger cloud patches, and iii) the inner-domain simulations (150 m, 300 m, and 500 m) do not differ strongly from the simulation which provides the boundary conditions (1.1 km). We have included this figure in the appendix because these data were produced using the same model setup but run on a different machine, so may not be bitwise comparable, and the satellite simulator was only run on a subset of times (11Z-21Z). There is also an additional 150 m-resolution simulation included that was not able to be run with the simulations used in the main paper.

## Appendix B Open Research

The model output is kept on the Met Office archiving system at “moose:/adhoc/projects/eurec4auk/moisture\_tracers/vn12.0/”. The modifications to the Unified Model code to include tracer diagnostics are on the branch leosaffin/r100515\_moisture\_tracers (revision 105047) in the Met Office repository. The code used for data analysis is available at “[https://github.com/leosaffin/moisture\\_tracers](https://github.com/leosaffin/moisture_tracers)”.

## Acknowledgments

EUREC4A funding: This work was funded by EUREC4A-UK (NE/S015868/1), Para-Con (NE/T003898/1) and UK Department for Business, Energy and Industrial Strategy. We acknowledge use of the Monsoon2 system, a collaborative facility supplied un-

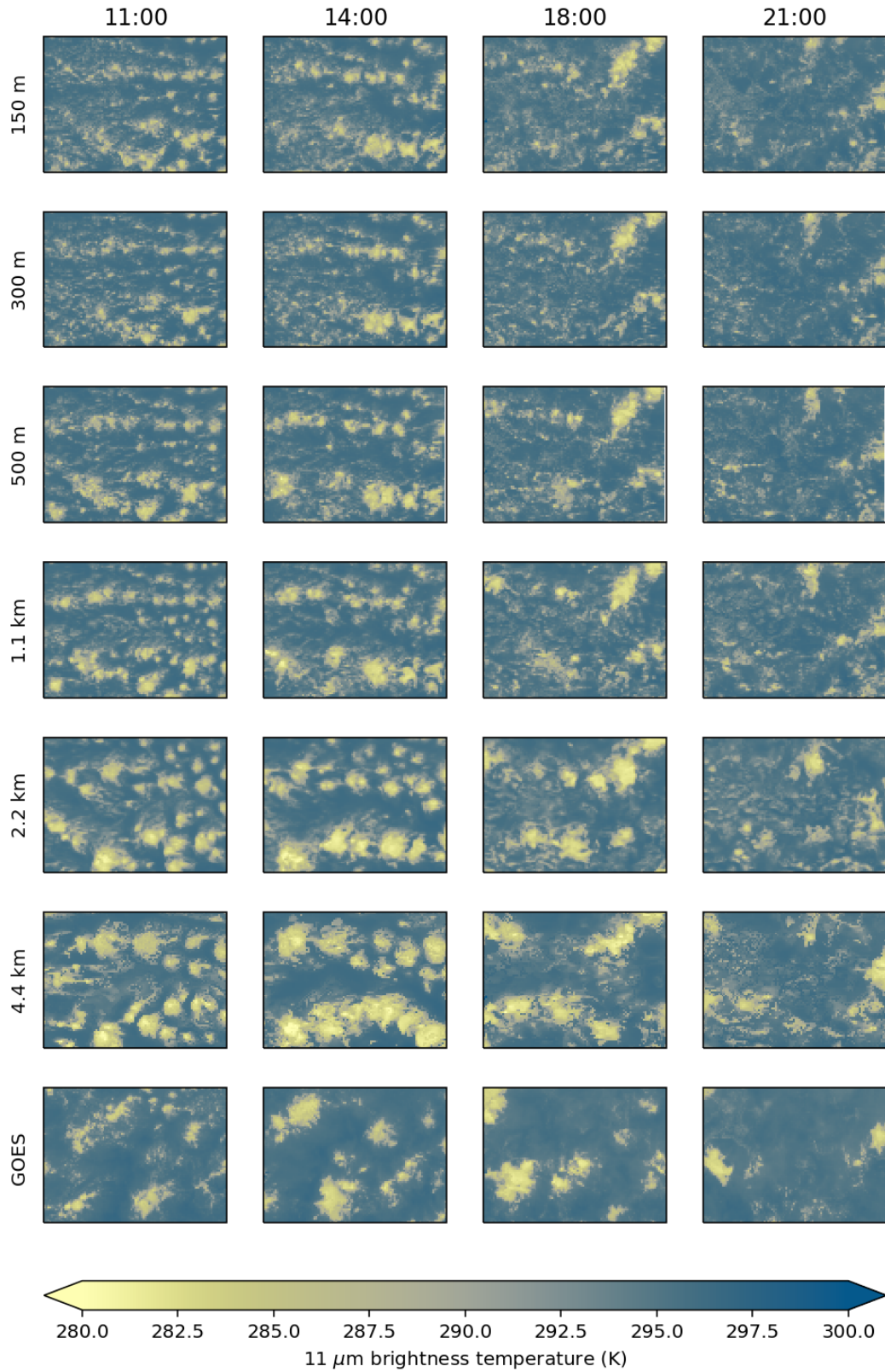


**Figure A1.** The same as Fig. 2 but with the model output shown as simulated 11  $\mu\text{m}$  brightness temperature and the output is shown for a different set of times (top header). This output comes from the same model setup but run on a different machine, so may not be exactly comparable.

der the Joint Weather and Climate Research Programme, a strategic partnership between the Met Office and the Natural Environment Research Council.

## References

- Bony, S., & Dufresne, J.-L. (2005). Marine boundary layer clouds at the heart of tropical cloud feedback uncertainties in climate models. *Geophysical Research Letters*, *32*. doi: <https://doi.org/10.1029/2005GL023851>
- Bony, S., Schulz, H., Vial, J., & Stevens, B. (2020, 1). Sugar, gravel, fish and flowers: Dependence of mesoscale patterns of trade-wind clouds on environmental conditions. *Geophysical Research Letters*, *n/a*, 2019GL085988. doi: [10.1029/2019GL085988](https://doi.org/10.1029/2019GL085988)
- Bony, S., Stevens, B., Ament, F., Bigorre, S., Chazette, P., Crewell, S., ... Wirth, M. (2017). Eurec4a: A field campaign to elucidate the couplings between clouds, convection and circulation. *Surveys in Geophysics*, *38*, 1529-1568. doi: [10.1007/s10712-017-9428-0](https://doi.org/10.1007/s10712-017-9428-0)
- Boutle, I. A., Eyre, J. E., & Lock, A. P. (2014, 4). Seamless stratocumulus simulation across the turbulent gray zone. *Monthly Weather Review*, *142*, 1655-1668. doi: [10.1175/MWR-D-13-00229.1](https://doi.org/10.1175/MWR-D-13-00229.1)
- Bretherton, C. S., & Blossey, P. N. (2017, 12). Understanding mesoscale aggregation of shallow cumulus convection using large-eddy simulation. *Journal of Advances in Modeling Earth Systems*, *9*, 2798-2821. doi: [10.1002/2017MS000981](https://doi.org/10.1002/2017MS000981)
- Brueck, M., Nuijens, L., & Stevens, B. (2015, 4). On the seasonal and synoptic time-scale variability of the north atlantic trade wind region and its low-level clouds. *Journal of the Atmospheric Sciences*, *72*, 1428-1446. doi: [10.1175/JAS-D-14-0054.1](https://doi.org/10.1175/JAS-D-14-0054.1)
- Bush, M., Allen, T., Bain, C., Boutle, I., Edwards, J., Finnenkoetter, A., ... Zerroukat, M. (2020, 4). The first met office unified model-jules regional atmosphere and land configuration, r11. *Geoscientific Model Development*, *13*, 1999-2029. doi: [10.5194/gmd-13-1999-2020](https://doi.org/10.5194/gmd-13-1999-2020)
- Denby, L. (2020, 1). Discovering the importance of mesoscale cloud organization through unsupervised classification. *Geophysical Research Letters*, *47*, e2019GL085190. doi: [10.1029/2019GL085190](https://doi.org/10.1029/2019GL085190)

- 660 Hanley, K., Whitall, M., Stirling, A., & Clark, P. (2019, 10). Modifications to  
661 the representation of subgrid mixing in kilometre-scale versions of the unified  
662 model. *Quarterly Journal of the Royal Meteorological Society*, *145*, 3361-3375.  
663 doi: 10.1002/QJ.3624
- 664 Hersbach, H., Bell, B., Berrisford, P., Hirahara, S., Horányi, A., Muñoz-Sabater,  
665 J., ... Thépaut, J.-N. (2020, 7). The era5 global reanalysis. *Quar-*  
666 *terly Journal of the Royal Meteorological Society*, *146*, 1999-2049. doi:  
667 <https://doi.org/10.1002/qj.3803>
- 668 Janssens, M., de Arellano, J. V., Scheffer, M., Antonissen, C., Siebesma, A. P.,  
669 & Glassmeier, F. (2021, 3). Cloud patterns in the trades have four inter-  
670 pretable dimensions. *Geophysical Research Letters*, *48*, e2020GL091001. doi:  
671 10.1029/2020GL091001
- 672 Kendon, E. J., Roberts, N. M., Fowler, H. J., Roberts, M. J., Chan, S. C., & Senior,  
673 C. A. (2014, jun). Heavier summer downpours with climate change revealed by  
674 weather forecast resolution model. *Nature Climate Change*, *4*(7), 570-576. doi:  
675 10.1038/nclimate2258
- 676 Kendon, E. J., Stratton, R. A., Tucker, S., Marsham, J. H., Berthou, S., Rowell,  
677 D. P., & Senior, C. A. (2019, apr). Enhanced future changes in wet and dry  
678 extremes over Africa at convection-permitting scale. *Nature Communications*  
679 *2019 10:1*, *10*(1), 1-14. doi: 10.1038/s41467-019-09776-9
- 680 Lock, A. P., Brown, A. R., Bush, M. R., Martin, G. M., & Smith, R. N. B. (2000,  
681 9). A new boundary layer mixing scheme. part i: Scheme description and  
682 single-column model tests. *Monthly Weather Review*, *128*, 3187-3199. doi:  
683 10.1175/1520-0493(2000)128<3187:ANBLMS>2.0.CO;2
- 684 Miltenberger, A. K., Field, P. R., Hill, A. A., Rosenberg, P., Shipway, B. J., Wilkin-  
685 son, J. M., ... Blyth, A. M. (2018, 3). Aerosol-cloud interactions in mixed-  
686 phase convective clouds - part 1: Aerosol perturbations. *Atmospheric Chem-*  
687 *istry and Physics*, *18*, 3119-3145. doi: 10.5194/ACP-18-3119-2018
- 688 Narenpitak, P., Kazil, J., Yamaguchi, T., Quinn, P., & Feingold, G. (2021). From  
689 sugar to flowers: A transition of shallow cumulus organization during atomic.  
690 *Journal of Advances in Modeling Earth Systems*, *13*, e2021MS002619. doi:  
691 <https://doi.org/10.1029/2021MS002619>
- 692 Nuijens, L., Medeiros, B., Sandu, I., & Ahlgrimm, M. (2015a, 6). The behavior of

- trade-wind cloudiness in observations and models: The major cloud components and their variability. *Journal of Advances in Modeling Earth Systems*, 7, 600-616. doi: 10.1002/2014MS000390
- Nuijens, L., Medeiros, B., Sandu, I., & Ahlgrim, M. (2015b, 12). Observed and modeled patterns of covariability between low-level cloudiness and the structure of the trade-wind layer. *Journal of Advances in Modeling Earth Systems*, 7, 1741-1764. doi: 10.1002/2015MS000483
- Nuijens, L., Serikov, I., Hirsch, L., Lonitz, K., & Stevens, B. (2014, 10). The distribution and variability of low-level cloud in the north atlantic trades. *Quarterly Journal of the Royal Meteorological Society*, 140, 2364-2374. doi: 10.1002/QJ.2307
- Saunders, R., Hocking, J., Turner, E., Rayer, P., Rundle, D., Brunel, P., ... Lupu, C. (2018, 7). An update on the rtov fast radiative transfer model (currently at version 12). *Geoscientific Model Development*, 11, 2717-2737. doi: 10.5194/GMD-11-2717-2018
- Slingo, J., Bates, P., Bauer, P., Belcher, S., Palmer, T., Stephens, G., ... Teutsch, G. (2022, jun). Ambitious partnership needed for reliable climate prediction. *Nature Climate Change*, 12(6), 499-503. doi: 10.1038/s41558-022-01384-8
- Sprenger, M., & Wernli, H. (2015, 8). The lagranto lagrangian analysis tool – version 2.0. *Geoscientific Model Development*, 8, 1893-1943. doi: 10.5194/gmdd-8-1893-2015
- Stevens, B., Bony, S., Brogniez, H., Hentgen, L., Hohenegger, C., Kiemle, C., ... Zuidema, P. (2020, 1). Sugar, gravel, fish and flowers: Mesoscale cloud patterns in the trade winds. *Quarterly Journal of the Royal Meteorological Society*, 146, 141-152. doi: 10.1002/qj.3662
- Stevens, B., Bony, S., Farrell, D., Ament, F., Blyth, A., Fairall, C., ... Zöger, M. (2021, 8). Eurec4a. *Earth System Science Data*, 13, 4067-4119. doi: 10.5194/ESSD-13-4067-2021
- Tomassini, L., Field, P. R., Honnert, R., Malardel, S., McTaggart-Cowan, R., Saitou, K., ... Seifert, A. (2017, 3). The “grey zone” cold air outbreak global model intercomparison: A cross evaluation using large-eddy simulations. *Journal of Advances in Modeling Earth Systems*, 9, 39-64. doi: 10.1002/2016MS000822
- Vial, J., Bony, S., Dufresne, J. L., & Roehrig, R. (2016, 12). Coupling between

- 726 lower-tropospheric convective mixing and low-level clouds: Physical mecha-  
 727 nisms and dependence on convection scheme. *Journal of Advances in Modeling*  
 728 *Earth Systems*, 8, 1892-1911. doi: 10.1002/2016MS000740
- 729 Vogel, R., Nuijens, L., & Stevens, B. (2019, 9). Influence of deepening and mesoscale  
 730 organization of shallow convection on stratiform cloudiness in the downstream  
 731 trades. *Quarterly Journal of the Royal Meteorological Society*, n/a. doi:  
 732 10.1002/qj.3664
- 733 Wernli, H., & Davies, H. C. (1997, 1). A lagrangian-based analysis of extratropical  
 734 cyclones. i: The method and some applications. *Quarterly Journal of the Royal*  
 735 *Meteorological Society*, 123, 467-489. doi: 10.1002/qj.49712353811
- 736 Weverberg, K. V., Morcrette, C. J., Boutle, I., Furtado, K., & Field, P. R. (2021,  
 737 3). A bimodal diagnostic cloud fraction parameterization. part i: Motivating  
 738 analysis and scheme description. *Monthly Weather Review*, 149, 841-857. doi:  
 739 10.1175/MWR-D-20-0224.1

Figure 1.

Total Column Water (500m and 1.1km)  
12Z 2<sup>nd</sup> Feb (T+36h)

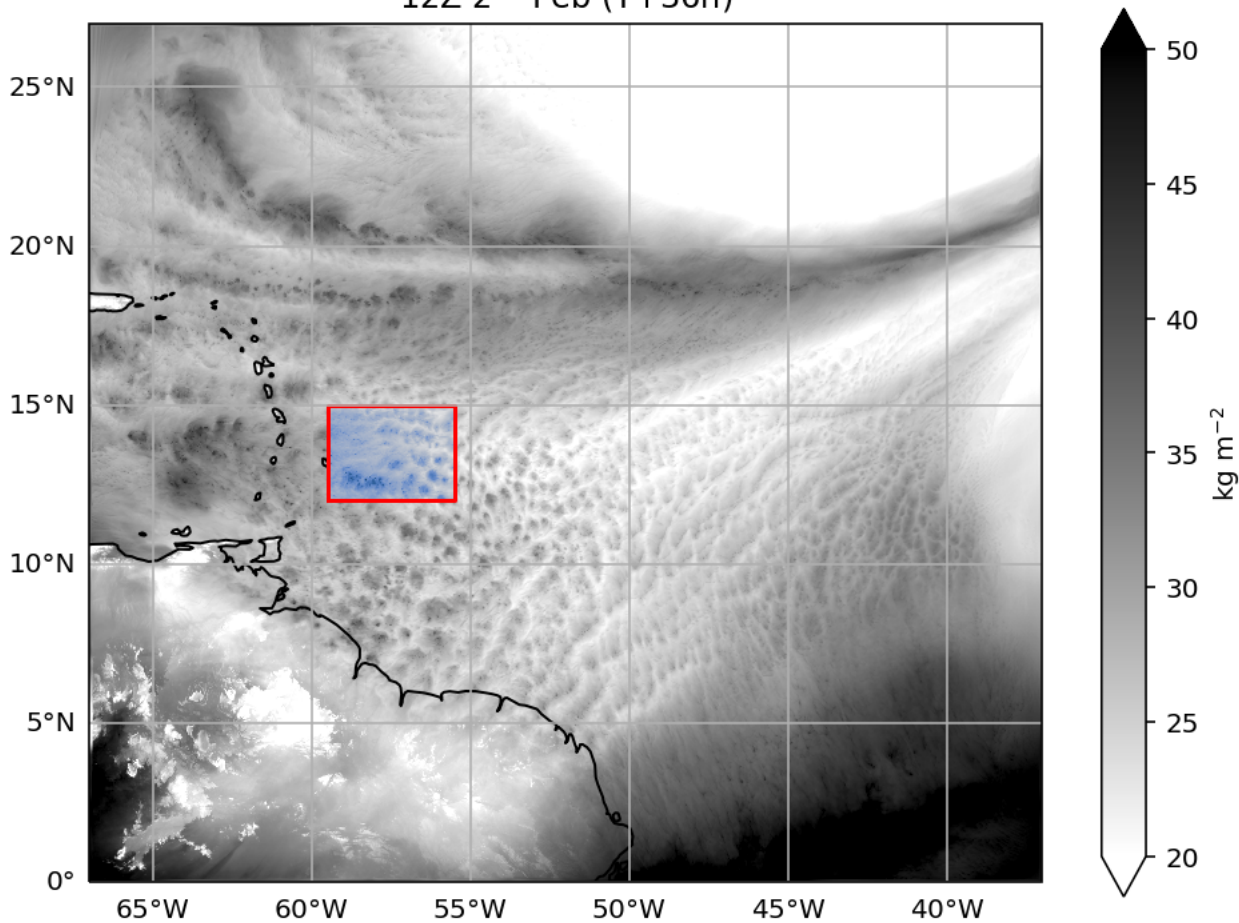


Figure 2.

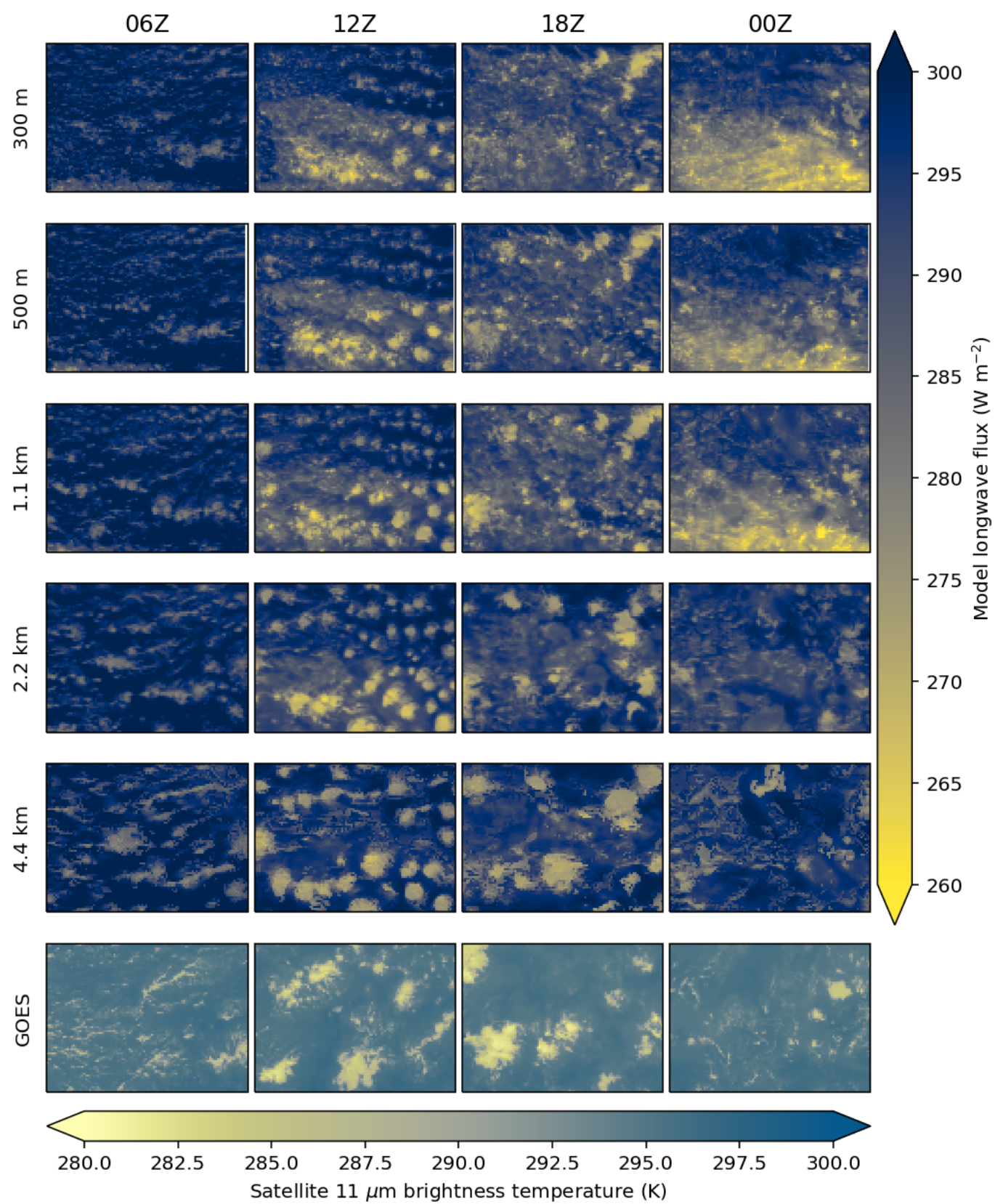


Figure 3.

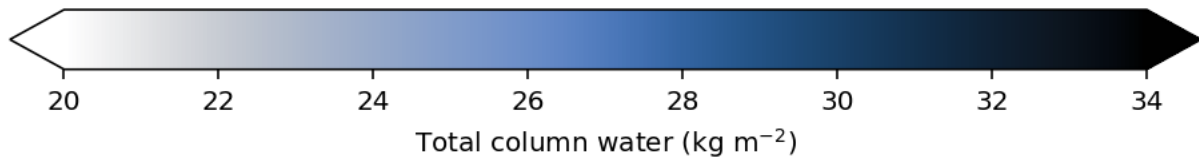
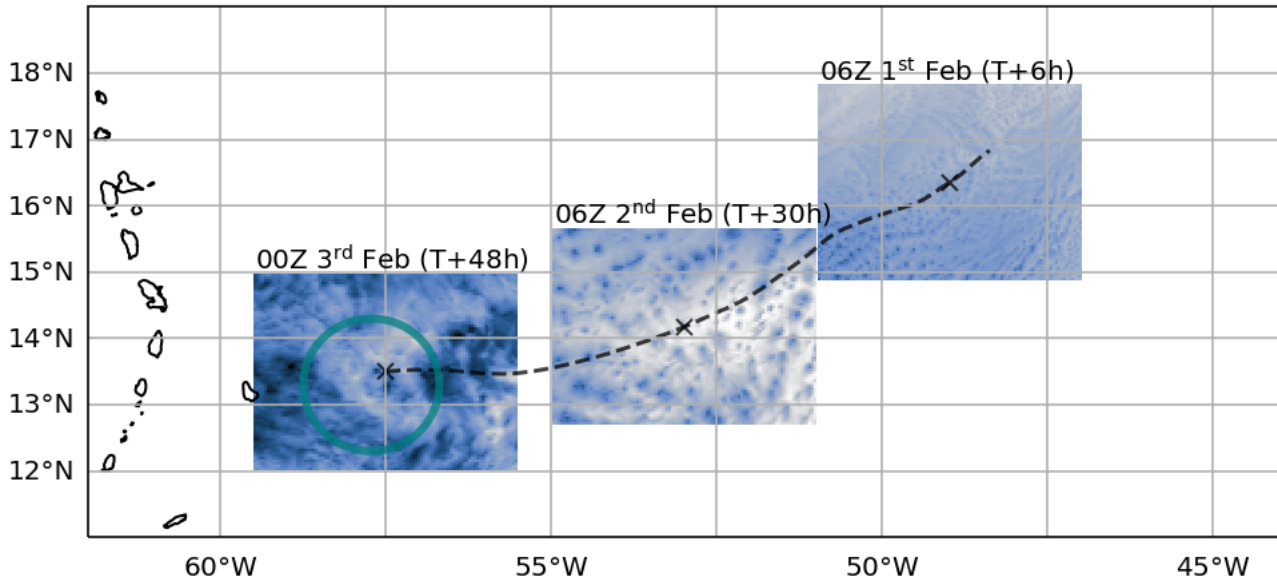


Figure 4.

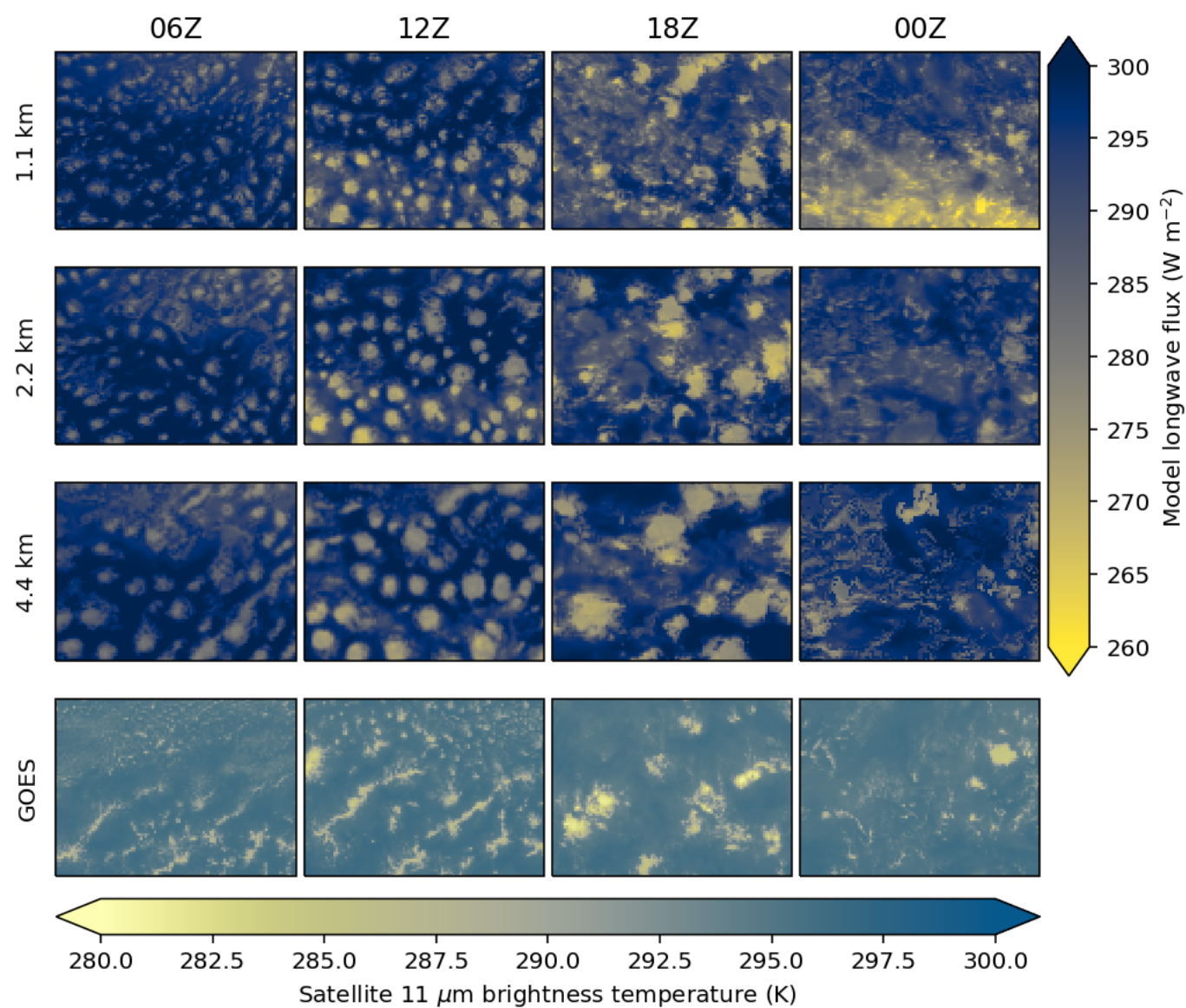
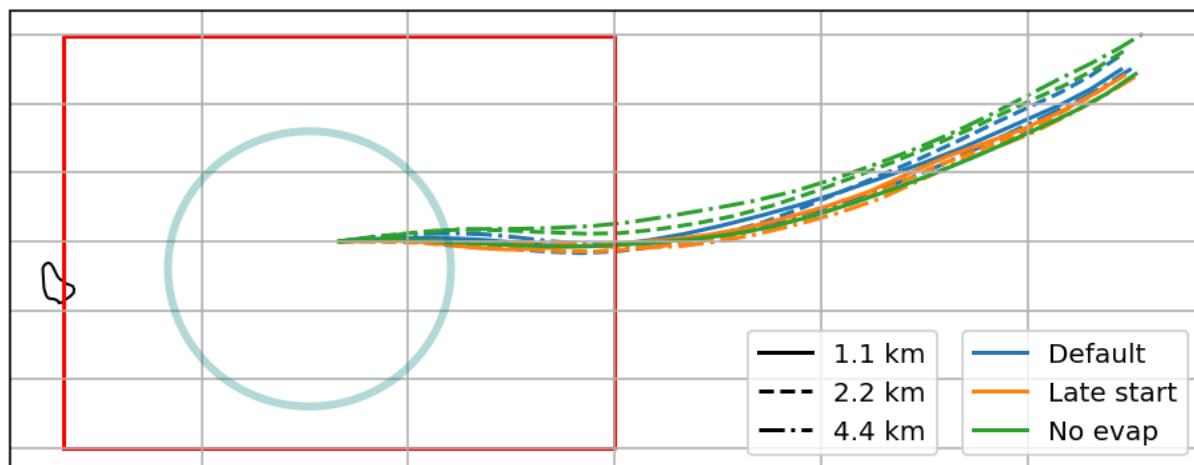


Figure 5.

(a)



(b)

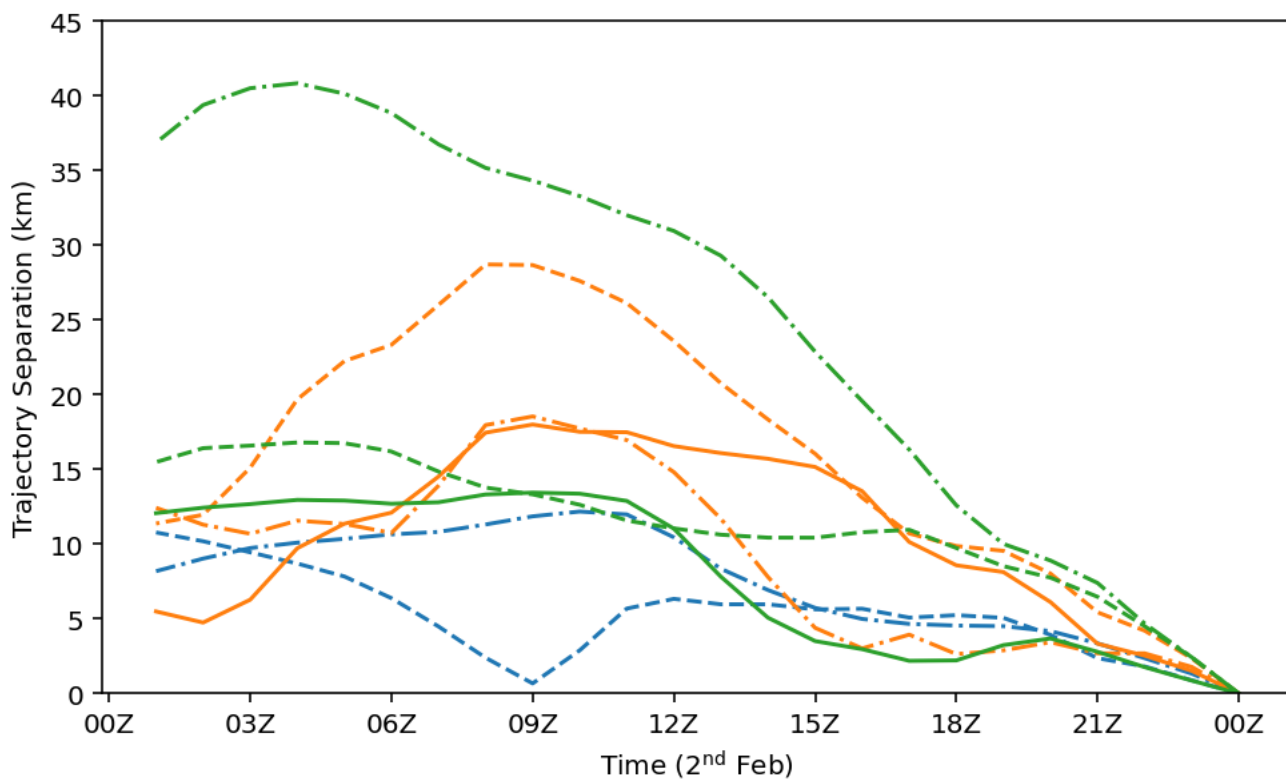
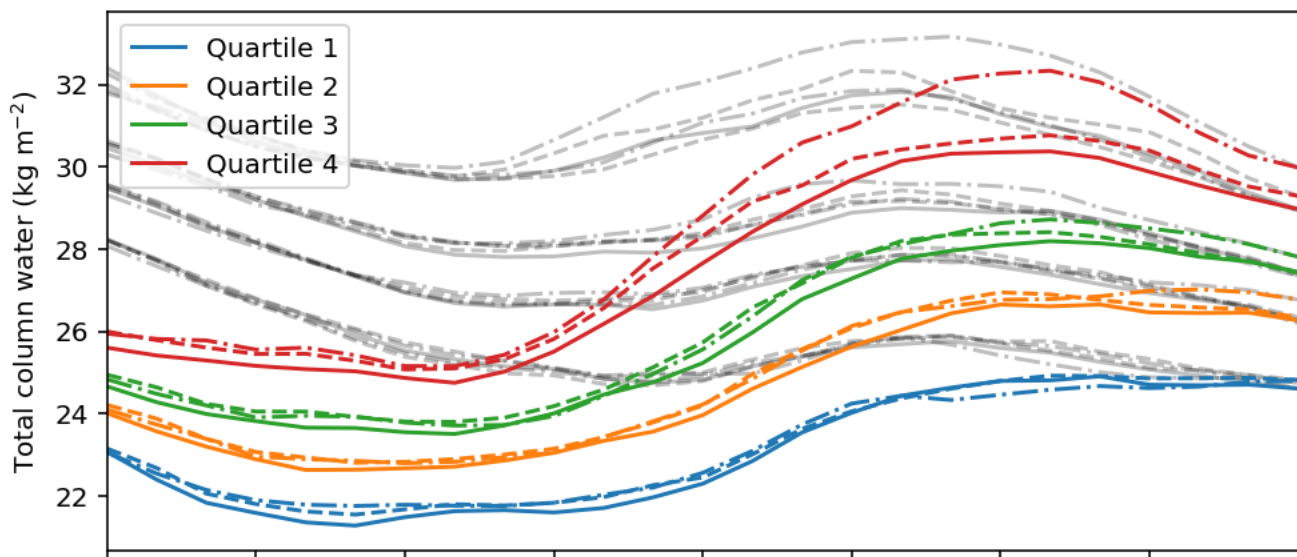


Figure 6.

(a)



(b)

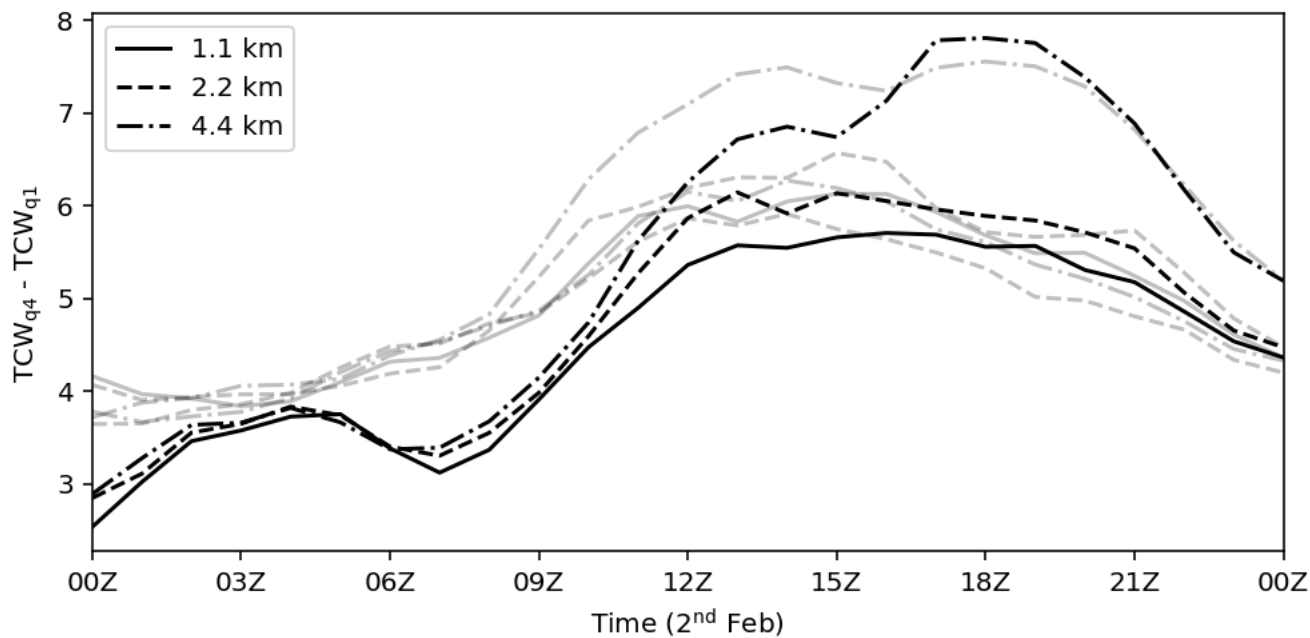


Figure 7.

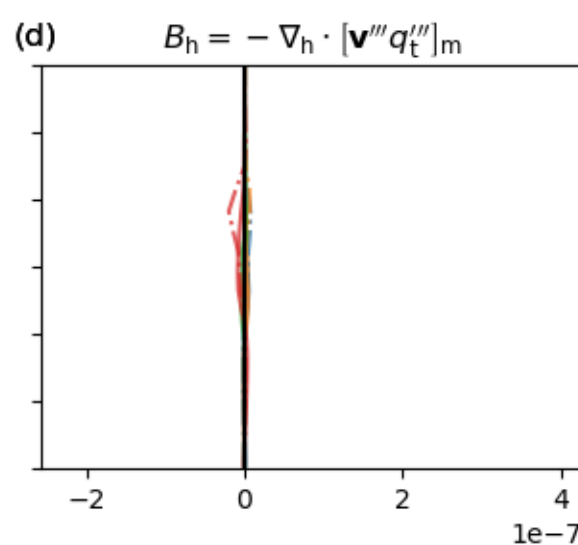
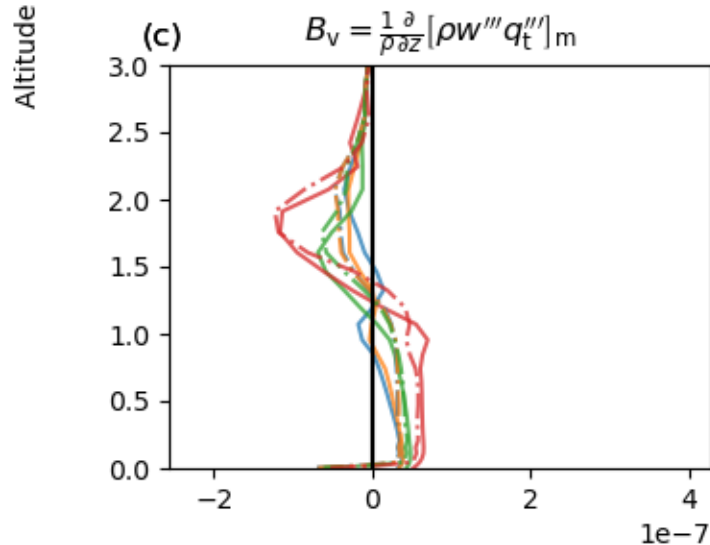
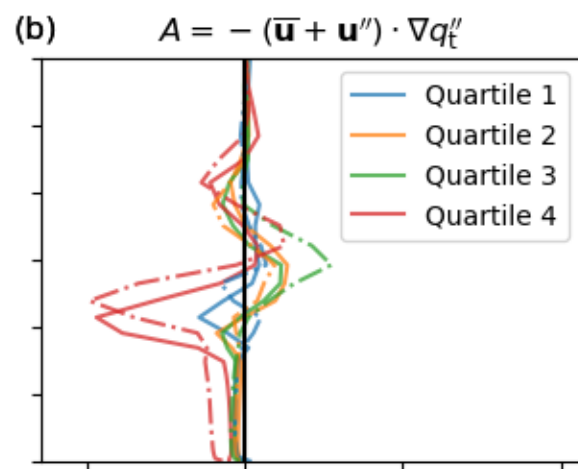
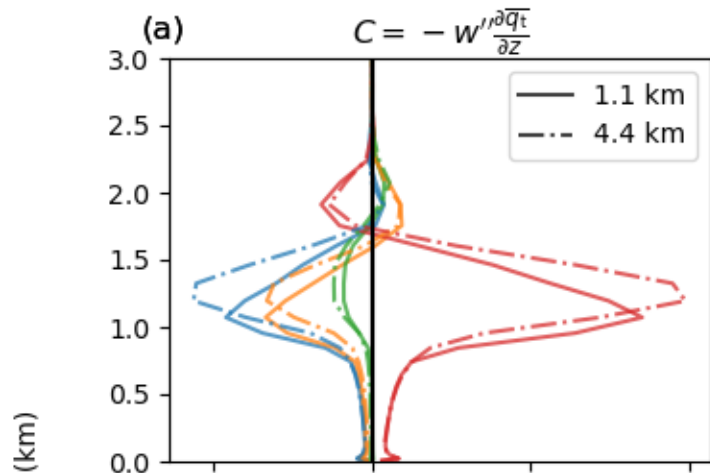
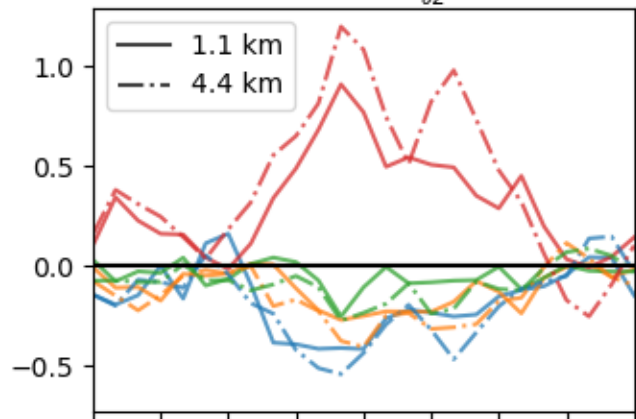


Figure 8.

Rate of change in mesoscale moisture anomaly ( $\text{kg m}^{-2} \text{hour}^{-1}$ )

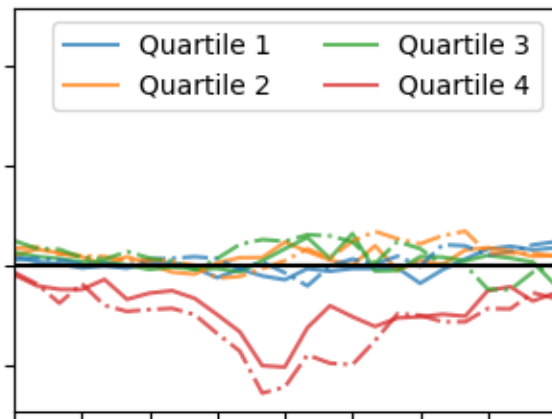
(a)

$$C = -w'''\frac{\partial \bar{q}_t}{\partial z}$$



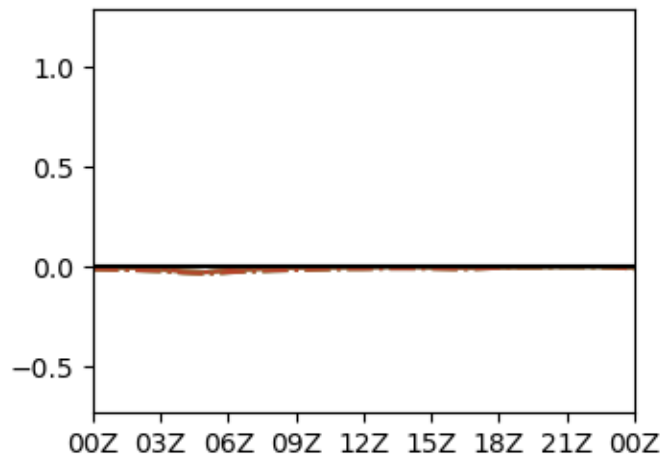
(b)

$$A = -(\bar{\mathbf{u}} + \mathbf{u}'') \cdot \nabla q_t''$$



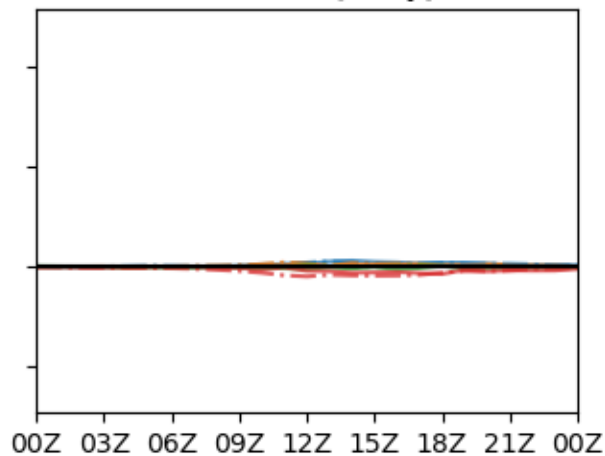
(c)

$$B_v = \frac{1}{\rho} \frac{\partial}{\partial z} [\rho w''' q_t''']_m$$



(d)

$$B_h = -\nabla_h \cdot [\mathbf{v}''' q_t''']_m$$

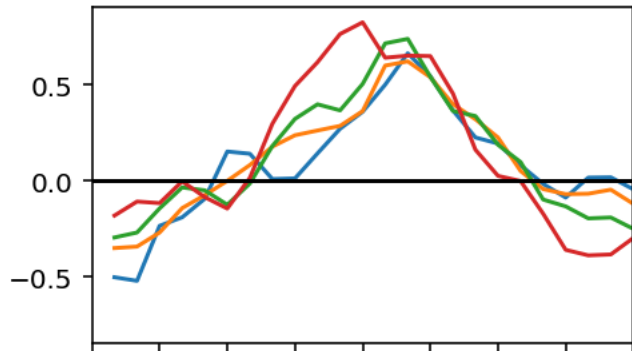


Time (2<sup>nd</sup> Feb)

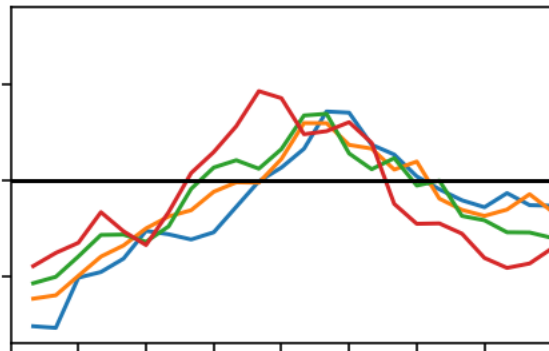
Figure 9.

Change in total column water ( $\text{kg m}^{-2} \text{ hour}^{-1}$ )

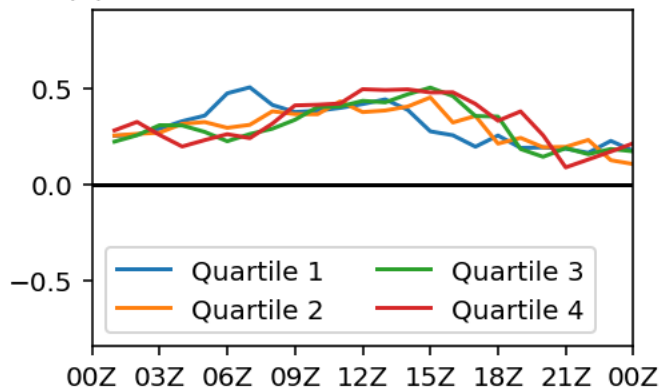
(a) Specific humidity



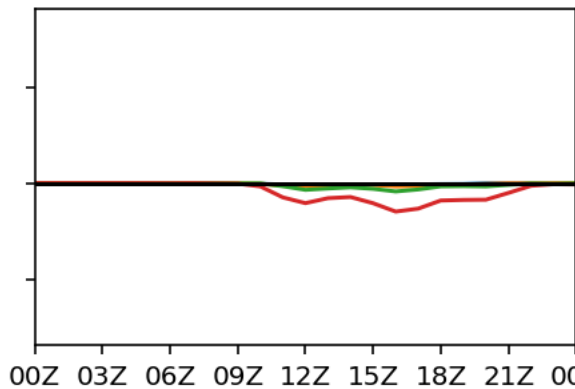
(b) Passive tracer



(c) Surface fluxes



(d) Rain

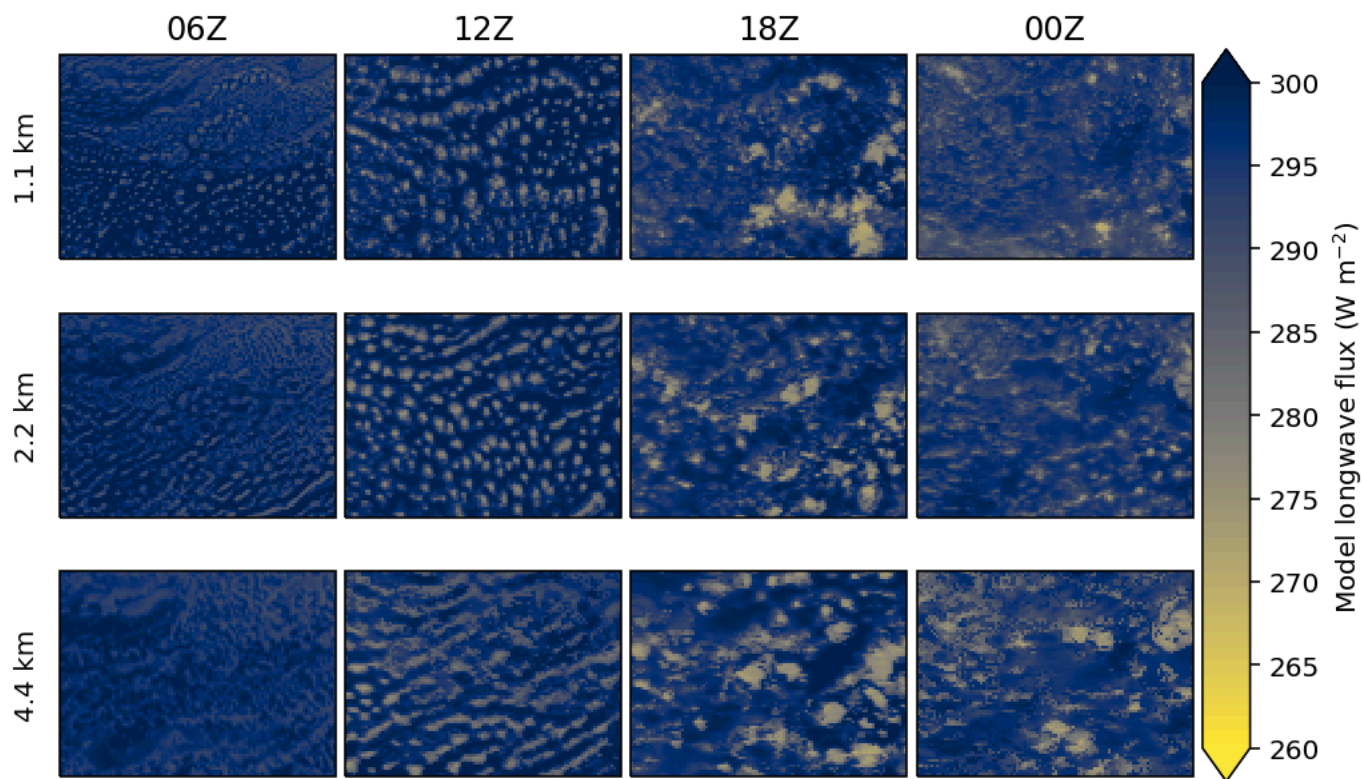


Time (2<sup>nd</sup> Feb)

Figure 10.

(a)

Late start



(b)

No Evap

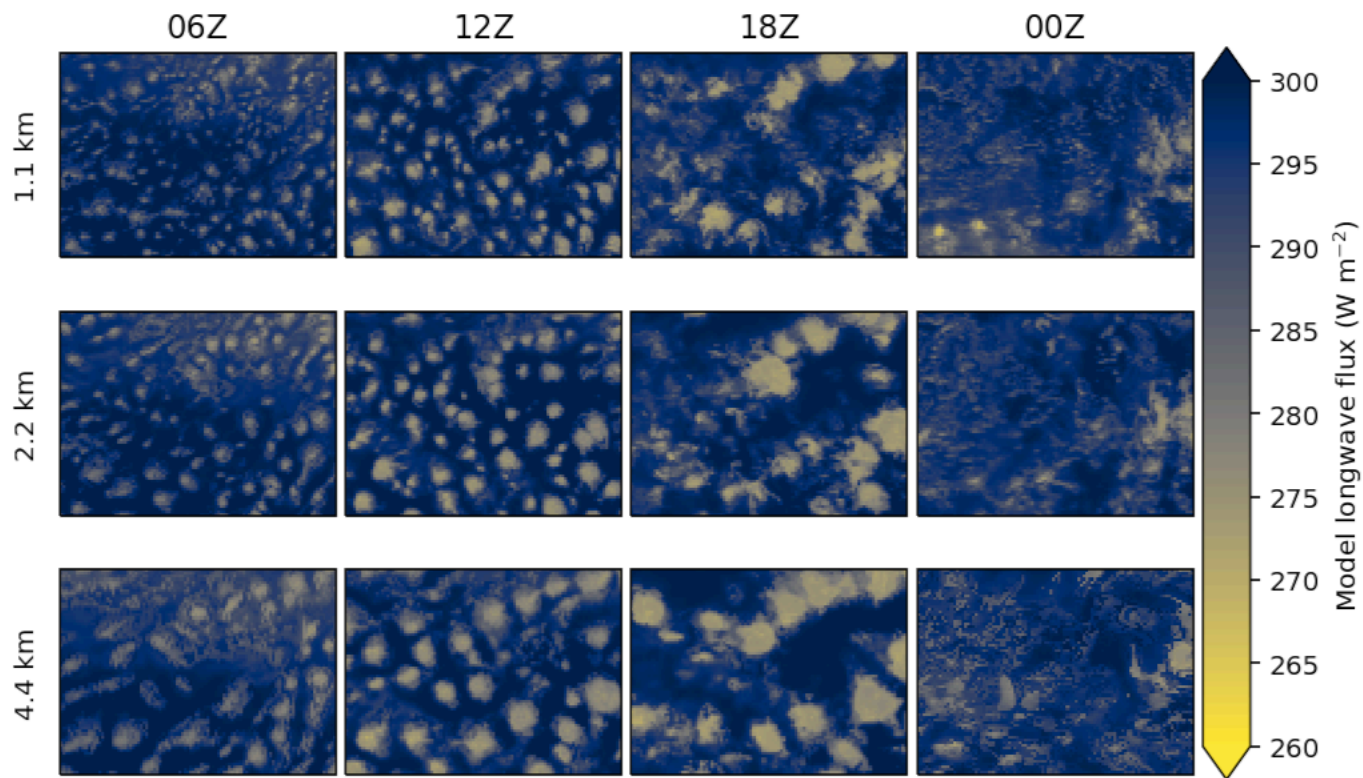
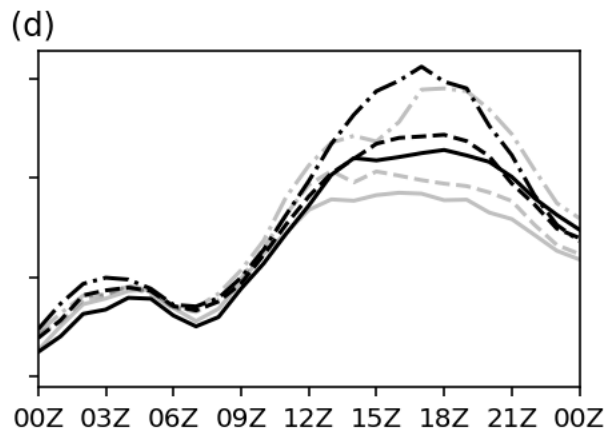
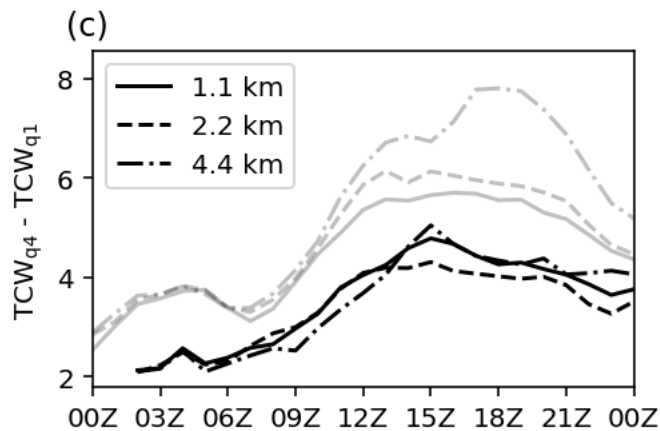
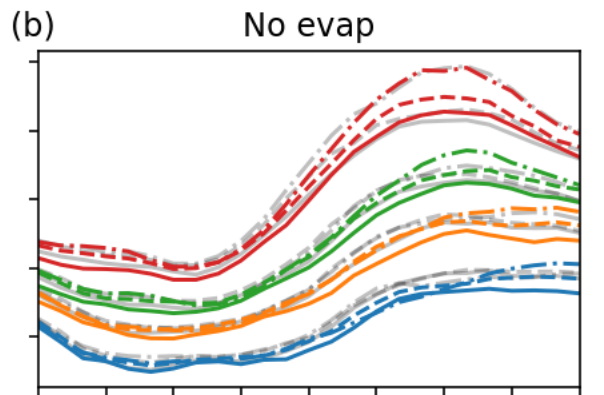
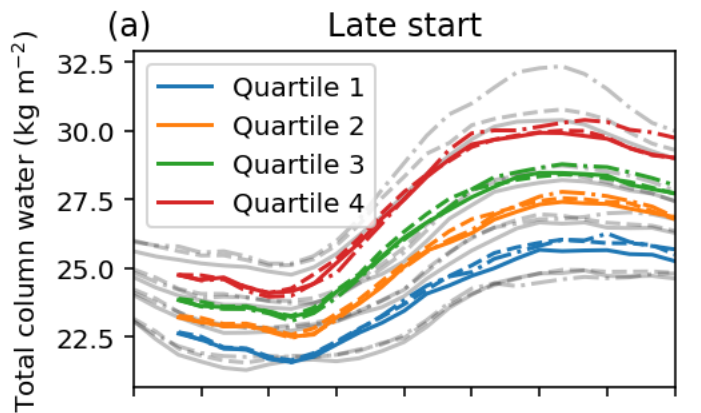


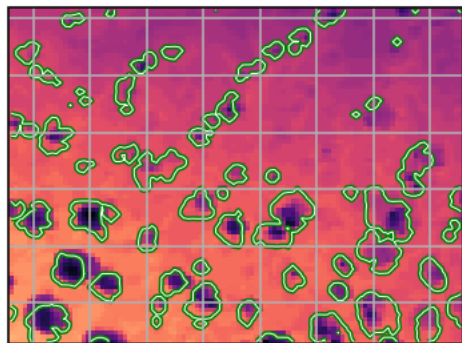
Figure 11.



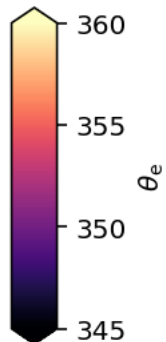
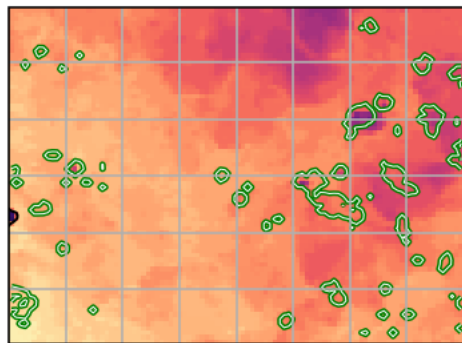
Time (2<sup>nd</sup> Feb)

Figure 12.

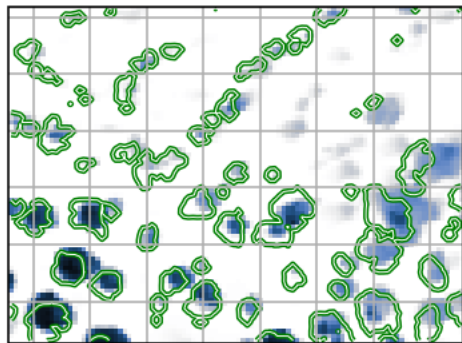
(a) 12Z 2<sup>nd</sup> Feb



(b) 00Z 3<sup>rd</sup> Feb



(c)



(d)

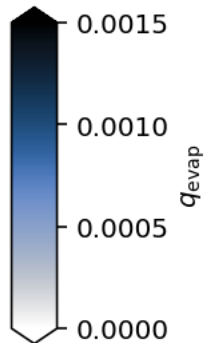
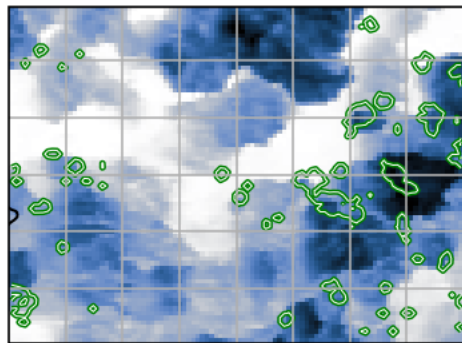


Figure 13.

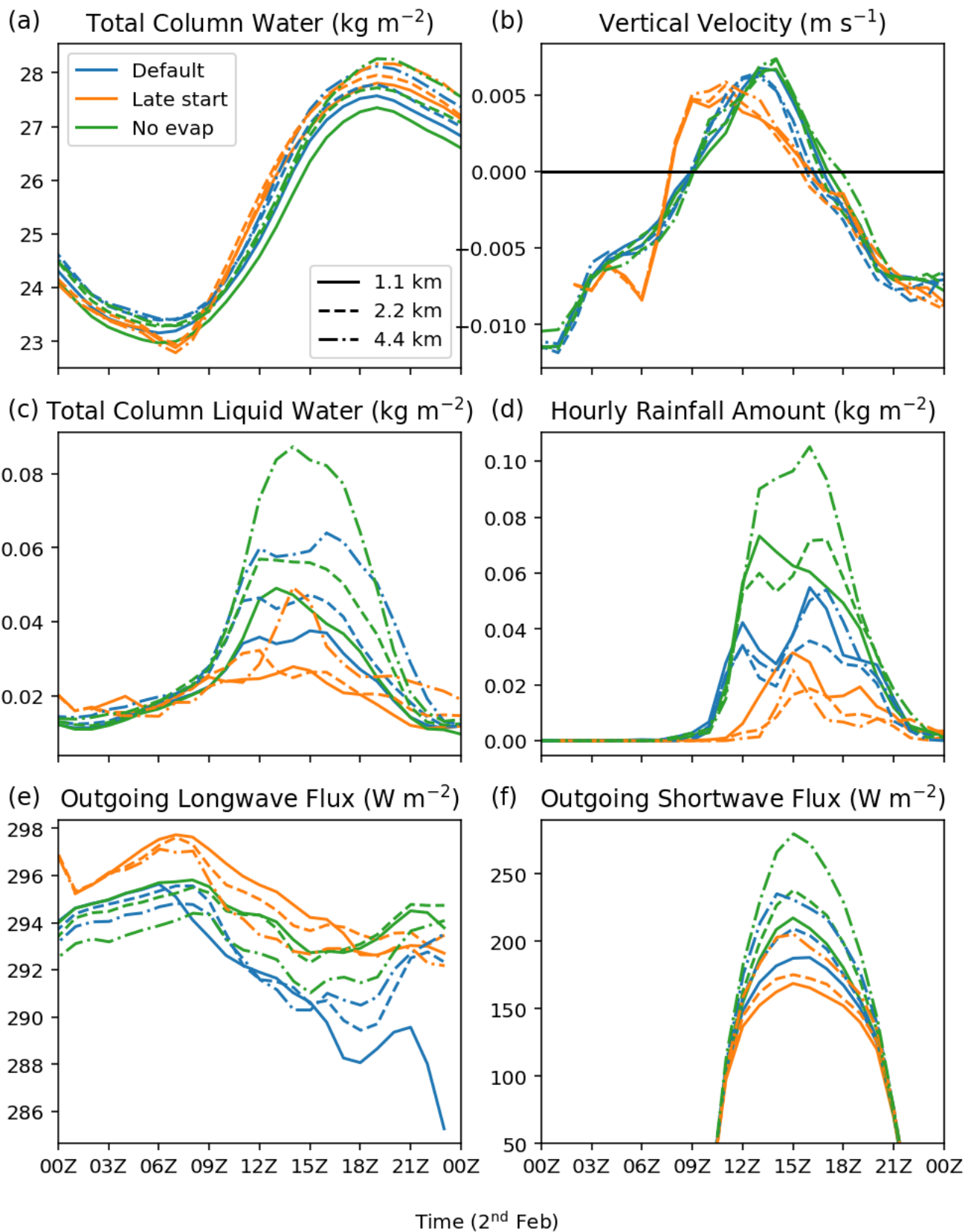


Figure A1.

